Remote Sensing of Environment 301 (2024) 113935

Contents lists available at ScienceDirect

Remote Sensing of Environment

journal homepage: www.elsevier.com/locate/rse

Arctic tundra shrubification can obscure increasing levels of soil erosion in NDVI assessments of land cover derived from satellite imagery

Georg Kodl [a,*], Richard Streeter [a], Nick Cutler [b], Tobias Bolch [c]

[a] School of Geography and Sustainable Development, University of St Andrews, UK
[b] School of Geography, Politics and Sociology, University of Newcastle, UK
[c] Institute of Geodesy, Graz University of Technology, Austria

ARTICLE INFO

Edited by Zhe Zhu

Keywords:
Soil erosion
Shrub expansion
Arctic tundra
Mixed pixel
NDVI
Shannon evenness index (SHEI)

ABSTRACT

Monitoring soil erosion in the Arctic tundra is complicated by the highly fragmentated nature of the landscape and the limited spatial resolution of even high-resolution satellite data. The expansion of shrubs across the Arctic has led to substantial changes in vegetation composition that alter the spectral reflectance and directly affect vegetation indices such as the normalized difference vegetation index (NDVI), which is widely applied for environmental monitoring. This change can mask soil erosion if datasets with too coarse spatial resolutions are used, as increases in NDVI driven by shrub expansion can obscure concurrent increases in barren land cover. Here we created land cover maps from a multispectral uncrewed aerial vehicle (UAV) and land cover survey and assessed satellite imagery from PlanetScope, Sentinel-2 and Landsat-8 for several areas in north-eastern Iceland. Additionally, we used a novel application of the Shannon evenness index (SHEI) to evaluate levels of pixel mixing. Our results show that shrub expansion can lead to spectral confusion, which can obscure soil erosion processes and emphasize the importance of considering spatial resolution when monitoring highly fragmented landscapes. We demonstrate that remote sensing data with a resolution < 3 m greatly improves the amount of information captured in an Icelandic tundra environment. The spatial resolution of Landsat data (30 m) is inadequate for environmental monitoring in our study area. We found that the best platform for monitoring tundra land cover is Sentinel-2 when used in combination with multispectral UAV acquisitions for validation. Our study has the potential to improve environmental monitoring capabilities by introducing the use of SHEI to assess pixel mixing and determine optimal spatial resolutions. This approach combined with comparing remote sensing imagery of different spatial and time scales significantly advances our comprehension of land cover changes, including greening and soil degradation, in the Arctic tundra.

1. Introduction

The Arctic tundra has warmed 2–4 times faster than the global average in recent decades (Rantanen et al., 2022; Post et al., 2019). This warming has led to profound ecological changes, including the encroachment of woody shrub species ('shrubification') with associated geomorphological changes (Kemppinen et al., 2021; Myers-Smith et al., 2011). Changes in vegetation composition and structure are likely to influence slope stability and processes of soil degradation/erosion and vice versa (Kemppinen et al., 2022; Eichel et al., 2016; Marston, 2010). However, uncertainties remain over the interaction between ecological and geomorphological processes in a rapidly changing climate (Niittynen et al., 2020; Lara et al., 2018). Large-scale changes in vegetation structure are commonly inferred from remote sensing data, notably the normalized difference vegetation index (NDVI), but these assessments are complicated by the interpretation of NDVI values (Giri et al., 2013). The calibration of remote sensing data with finer-resolution imagery derived from uncrewed aerial vehicles (UAVs) offers a way forward. This paper addresses the interpretation of NDVI values derived from satellite platforms by comparing high- to mid-resolution remote sensing NDVI scenes from Landsat-8 (L8, spatial resolution 30 m), Sentinel-2 (S2, 10 m) and PlanetScope (PS, 3 m) with collected very-high-resolution (0.05 m) multispectral data acquired using a UAV. In addition, the effect of different scales on the spectral

* Corresponding author at: School of Geography and Sustainable Development, University of St Andrews, Irvine Building North Street, St Andrews KY16 9AL, Scotland, UK.
E-mail addresses: gk66@st-andrews.ac.uk (G. Kodl), rts3@st-andrews.ac.uk (R. Streeter), nick.cutler@ncl.ac.uk (N. Cutler), tobias.bolch@tugraz.at (T. Bolch).

https://doi.org/10.1016/j.rse.2023.113935
Received 9 August 2023; Received in revised form 13 November 2023; Accepted 27 November 2023
Available online 12 December 2023
0034-4257/© 2023 The Author(s). Published by Elsevier Inc. This is an open access article under the CC BY license (http://creativecommons.org/licenses/by/4.0/).

mixture of pixels is tested by using classified landscapes from the UAV images.

Satellite monitoring indicates widespread long-term greening trends across a majority of the circumpolar Arctic within the period (1982–2017), reflecting an increase in vegetation productivity (Bhatt et al., 2017; Ju and Masek, 2016; Xu et al., 2013), and in some cases a shift in plant dominance, in particular to an increase in shrub biomass (Weijers et al., 2018; Forbes et al., 2010).

A warmer, wetter climate is likely to lead to the expansion of shrubs with upright growth forms in the tundra ('shrubification': Myers-Smith and Hik, 2018; Martin et al., 2017; Tape et al., 2012), as growth conditions ameliorate. It is estimated that > 50% of the tundra biome will be replaced by woody shrubs by 2050 (Meredith et al., 2019). Shrubification will result in increased canopy cover and woody root mass, which will reduce surface wind speeds, intercept rainfall and bind soils to the substrate. These processes would tend to reduce soil erosion. The magnitude of this effect is not yet clear (Heindel et al., 2017); it is therefore essential to monitor shrubification if we are to understand geomorphological changes – including soil erosion – and ecological changes including vegetation cover in high-latitude areas.

Soil erosion is a major problem in Iceland, due to a combination of fine, low cohesion soils, high winds, grazing pressure and frequent freeze thaw cycles (Dugmore et al., 2009; Arnalds, 2015). Vegetation cover is a particularly important control on erosion rates, because plants have the potential to retard soil loss. A key metric is the ratio of vegetated to eroded area (Streeter and Cutler, 2020; Barrio et al., 2018; Thorsson, 2008). At critically low values of this ratio, a tipping point may be reached and rapid soil erosion can lead to irreversible desertification (Rietkerk et al., 2004).

The obvious way to measure large-scale changes in tundra cover is remote sensing, but the unique characteristics of tundra landscapes complicate the estimation of land cover change. Tundra ecosystems are highly fragmented compared to other biomes (Virtanen and Ek, 2014). They consist of a mosaic of different vegetation, geomorphic formations and water bodies and are characterised by multiple scales of landscape heterogeneity (Stow et al., 2004; McFadden et al., 1998). This heterogeneity is a result of combined factors related to the harsh Arctic climate. The sparse vegetation cover is susceptible to physical forces such as wind and frost activity. Combined with seasonal and longer-term changes, it affects soil properties and cause small-scale variations in vegetation and land cover (Virtanen and Ek, 2014).

The most commonly used indicator of photosynthetic activity is the NDVI, as it can be easily calculated from the near-infrared (NIR) and red spectral bands, which have been observed from space since the 1970s (Myers-Smith et al., 2020). The applicability of NDVI for the detection of vegetation cover has been demonstrated in the Arctic and Antarctic environments (Sotille et al., 2020; Fretwell et al., 2011; Laidler et al., 2008). Yang et al. (2020) suggest that deciduous shrub cover has a significant impact on spectral reflectance, particular in the NIR range. Increases in shrub cover should lead to higher NIR reflectance; in contrast, eroded terrain will have much lower values. The use of NDVI to infer land surface change may therefore be complicated if shrubification occurs at the same time as soil erosion. In this scenario, increased shrub vitality (and higher NIR reflectance) might mask an increase in eroded terrain (with an associated decrease in NIR reflectance) (Fig. 1).

As Fig. 1 demonstrates, large-scale Arctic monitoring studies run the risk of inferring the wrong ecological trends from datasets with coarse spatial resolution. In the study of Ju and Masek (2016) in Canada and Alaska, NDVI trend analysis between AVHRR and Landsat showed broadly similar large scale trends but differed considerably from regional trend patterns. Siewert and Olofsson (2020) showed in a study for northern Sweden that when decreasing resolution from UAV imagery to satellite scale, the mean NDVI remained stable, but the biomass and gross primary productivity (GPP) calculated from NDVI were underestimated due to non-linear relationship between remote sensing products, ecosystem processes, and spatial heterogeneity. Similarly, research

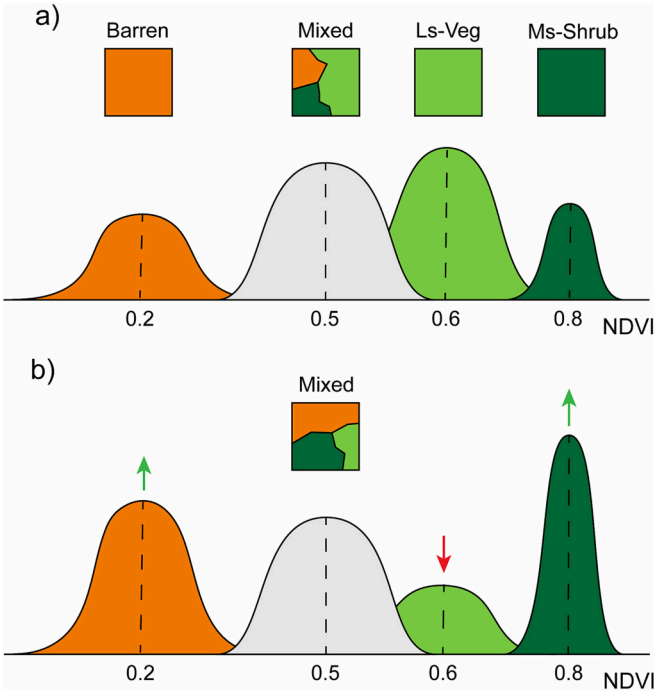

Fig. 1. Spectral confusion caused by mixing of land cover types. a) The three functional land cover type Barren, Low-stature Vegetation (Ls-Veg) and Medium-stature Shrub (Ms-Shrub) are contributing to the spectral mixing of a sensed pixel shown in grey. b) Barren and Ms-Shrub cover is increasing over time while Ls-Veg cover decreases, but the pixel NDVI value stays the same. Simultaneous changes in cover composition may mask each other, thereby impeding observations of land cover change at coarse spatial resolution (after Campbell, 2011).

from Assmann et al. (2020) in Herschel Island, Canada, revealed that the peak in spatial variation is around 0.5 m, at which resolution ecological information within plant communities are studied best. When upscaling to moderate grain resolution (~10–30 m) (i.e., those typically returned by satellite platforms), vital information was lost.

It is still not well understood how spatial aggregation influences the observed ecological heterogeneity in the various Arctic environments (Beamish et al., 2020). The spatial resolution and sensors used for monitoring are fundamentally related to how we can see and interpret the Earth's surface. One way to address the issues associated with coarse-scale satellite measurements, is to calibrate readings with fine-scale observations acquired from UAVs. Reduction in the size and cost of UAVs has made them more accessible to the research community, allowing the acquisition of very-high-resolution and radiometrically corrected multispectral imagery in remote areas. These data can be used together with field knowledge to compare and evaluate the validity of satellite products.

The major aim of our study is to understand how scale and sensor can affect estimations of vegetation cover. We suspected that ongoing soil erosion would not be visible in coarse-scale satellite data, due to climate-driven increases in photosynthetic activity. To investigate this, we carried out a multispectral UAV survey in 2021 at an actively eroding tundra rangeland in Iceland. We conducted a land cover classification from UAV imagery and compared the land cover maps to high- to mid-resolution (3–30 m) satellite imagery. Finally, we explored how different spatial resolutions affect spectral mixture and the consequent information loss, aiming to identify optimal spatial resolutions required for effective monitoring of the Arctic tundra.

2. Study site

The research was conducted at 12 study sites of 300 × 300 m, located in NE-Iceland (Fig. 2a). Sites were selected based on the criteria of low topographic variation, homogeneous vegetation cover, and similar hydrologic conditions. We aimed to cover areas in different degradation stages (Fig. 2b). The surveyed sites are located within unfenced rangelands. During the grazing season (May–September) sheep roam freely across these rangelands, except for the As-farm site, where grazing is only practiced in late summer. Sheep numbers across Iceland have declined hugely from a peak in the late 1970s, and we believe that our sites exhibited a similar trend (Marteinsdóttir et al., 2017). Consequently, stocking densities are low: we rarely saw sheep during our fieldwork and if we did, they were in small groups of just a few individuals.

The closest weather station is located in Raufarhöfn, about 30 km NW from the study sites (NE for site As). During the observation period between 1949 and 2008 the mean annual temperature was 2.5 °C and the mean annual precipitation 680 mm, both with an increasing trend since 1980s (Veðurstofa Íslands, 2022) (Fig. A1 in Appendix).

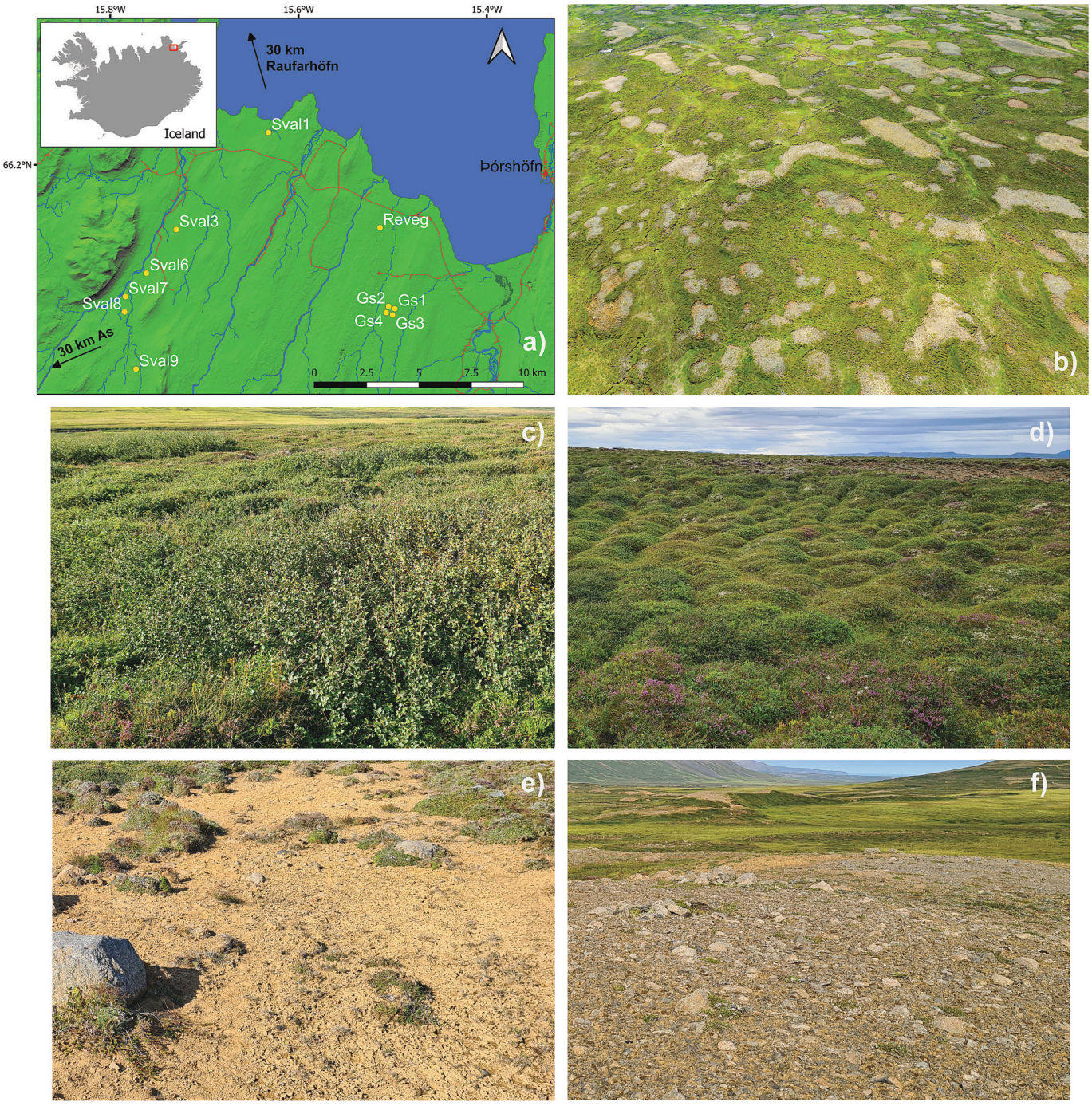

Fig. 2. a) Location of study sites surveyed in 2021 in NE-Iceland. b) UAV photo taken around location Gs2, showing a mosaic of eroded area (light tone) and tundra vegetation. c) Ms-Shrub land cover class with uniform patches of taller growing dwarf birch. d) Homogenous Ls-Veg land cover class showing a mixture of graminoids, forbs, low-stature shrubs, moss and lichen. e) Barren land cover with exposed Andosols in the foreground and remnant vegetation cover. f) Deflated barren land cover with rock debris and recolonising vegetation. (Photos taken by Georg Kodl).

The study area is located within the low-shrub tundra sub-zone (Walker et al., 2005). The tundra community is dominated mainly by medium-stature deciduous shrubs below 60 cm in height, mostly dwarf birch (*Betula nana*) (Fig. 2c). Also notable is the low-growing deciduous bog bilberry (*Vaccinium uliginosum*) and evergreen crowberry (*Empetrum nigrum*). Dwarf willow (*Salix herbacea*) is present but rarer due to grazing. Non-shrubby plants include graminoids (sedges, grasses and rushes), forbs, mosses and lichen (Fig. 2d). Plant community composition and susceptibility to erosion is strongly controlled by metre-scale mesotopographic variation (slope, topographic position index, aspect, elevation), which influences hydrology, snow cover, wind exposure and other environmental variables.

The landscape has a multi-scale topographical structure. In the range of 0.5–1 km radius, the lower elevated areas are waterlogged peatlands dominated by graminoids, while the higher elevated areas exhibit typical mixed tundra vegetation and have eroded surfaces. The higher elevated areas are further structured into undulating mounds with a diameter of 20–100 m and a height of 1–3 m, and small-scale dome-shaped mounds (Icelandic: thúfur) of about 0.5 m in diameter and 0.3 m in height, formed by cryoturbation.

The studied landscape is characterised by numerous erosion patches, ranging in size from 1 cm^2 to 100s m^2, embedded in a tundra vegetation matrix (Fig. 2b). The larger erosion patches can be stable over long periods of time from decades to centuries (Streeter and Cutler, 2020). Soils in this area of Iceland are Andosols, which mainly derive their properties from volcanic ejecta. They have a high-water retention capacity and are particularly susceptible to disturbances such as cryoturbation and aeolian erosion (Arnalds, 2015). Actively deflating areas consist of silt-sized soil particles, with remnants of vegetation cover but no secondary vegetation regrowth (Fig. 2e). Fully deflated areas consist of glacial till and have a darker appearance (Fig. 2f). On this eroded cover, recolonising vegetation is commonly established between or below the larger debris, mainly stress resistant vegetation as lichen, moss, biocrust and to a smaller extent, graminoids and low-growing shrubs.

3. Materials and methods

3.1. Satellite data

We compared Landsat-8 (L8), Sentinel-2 (S2), and PlanetScope (PS) satellite data with higher resolution data acquired with a UAV (Table 1). Cloud or haze free scenes were selected that were closest to the UAV acquisition period (Table A1 in Appendix). All downloaded scenes were analysis-ready orthorectified products, representing bottom of atmosphere reflectance images (Level 2, Table A2 in Appendix).

Furthermore, we used Landsat-5/7/8 imagery to plot a NDVI time series, to test whether continuous soil erosion is evident in the surveyed sites from 1984 until 2022. We extracted Landsat Collection 2 Tier 1 TOA reflectance data, which are most suitable for time series analysis, using Google Earth Engine (GEE) Code Editor (Table A3 in Appendix). The sensor range differ from Landsat-5/7 and Landsat-8 for the NIR band, but Collection 2 post-processed products are well radiometrically characterised and inter-calibrated across the different Landsat instruments (Landsat collection 2, 2021).

3.2. NDVI and aerial imagery trends

To understand vegetation trends in our study region we calculated the mean NDVI for each site considering only the growing season from June to September between 1984 and 2022.

Each script used for GEE included a feature collection that extracts data from each site on a specific date, a function that calculates the mean NDVI and a mask function that excludes all classified 'Cloud', 'Cloud Shadow', 'Dilated Clouds' and 'Cirrus' pixels from the provided '*QA_Pixel*' band. NDVI values < 0 were excluded. Datapoints that had values < 0.3 NDVI were manually checked to account for scenes that were not filtered by the cloud mask. Over 90 datapoints were excluded due to cloud coverage or georeferencing issues found in L5 data.

3.3. Multispectral UAV data collection

A UAV survey with a multispectral camera was conducted across the study area, in the later part of the growing season (23 Aug – 2 Sept 2021). A DJI Phantom 4 multispectral (P4m) quadcopter was used, which is equipped with a Blue (B) (450 nm ± 16 nm); Green (G) (560 nm ± 16 nm); Red (R) (650 nm ± 16 nm); Red-edge (RE) (730 nm ± 16 nm); Near-infrared (NIR) (840 nm ± 26 nm) sensor. Flight planning and execution followed the recommendations of the HiLDEN drone network protocol (Assmann et al., 2019). A reflectance target (Mapir Inc., San Diego) was imaged before, during and after the survey for radiometric calibration. Six to eight ground control points (GCPs) were selected prior to the flight and geolocated with a Spectra Precision ProMark 120 GPS system (Spectra Geospatial, Westminster CO).

The survey was flown along parallel flight and at an above ground altitude of 70 m, resulting in an average ground sampling distance of ~ 4 cm. Images were acquired with 80% front and side overlap and 2 h time difference to solar noon. Site Gs4 was surveyed in the morning due to time constraints, resulting in considerable shading effects from thúfurs. Survey details and weather conditions during each flight were recorded (Table A4 in Appendix) (UAV survey details in Appendix).

The UAV data were processed in Pix4D Mapper (Pix4D SA, Switzerland). Photogrammetric procedures were applied along with georeferencing based on the GCPs and radiometric calibration based on photographs of the calibration targets. The processed output comprised a digital surface model (DSM) and orthomosaics for each individual

Table 1
Characteristics of the remote sensing platforms used in the study. Scene identifiers used for the analysis can be found in the Appendix.

Remote sensing imagery metadata						
Platform	Phantom 4 m	PlanetScope	Sentinel-2	Landsat-8	Landsat-7	Landsat-5
Sensor	/	PSB.SD	MSI	OLI	ETM+	TM
Spatial resolution	0.05 m	3 m	10 m	30 m	30 m	30 m
Processing level	/	L3B	L2A	L2	L2	L2
Band Red	650 ± 16 nm	665 ± 15 nm	665 ± 15 nm	660 ± 13 nm	660 ± 30 nm	660 ± 30 nm
Band NIR	840 ± 26 nm	865 ± 20 nm	833 ± 53 nm	865 ± 14 nm	835 ± 65 nm	830 ± 70 nm
Radiometric resolution	16-bit	12-bit collected (scaled to 16-bit)			8-bit	8-bit
Repeated coverage	/	Daily	5 days	8 days[1]	16 days	16 days
Zenith view angle	0°	1–5°	7.7°	0°	0°	0°
In operation	/	Since 2016	Since 2015	Since 2013	Since 1999	1984–1995
Equatorial crossing[2]	11:00–15:30[3]	9:30–11:30	10:30	10:00	10:00	9:45

[1] with Landsat 9 since October 2021.
[2] Solar noon at study site 13:00.
[3] UAV acquisition time.

band. Furthermore, the NDVI was calculated as the normalized difference between the NIR and red band:

$$NDVI = \frac{NIR - Red}{NIR + Red} \quad (1)$$

3.4. Land cover classification and landscape characteristics

The aim of the land cover classification is to distinguish the following land cover categories: barren, mixed low-stature vegetation (including moss, lichen, graminoid, forbs, low-stature shrubs) and medium-stature shrub (namely *Betula nana* or dwarf birch). These classes were chosen to investigate the impact of the dwarf birch, a characteristic shrub of the Arctic tundra, on the overall spectral mix of the landscape, as this species has a high NDVI compared to other vegetation and spreads extensively. An advantage is that the dwarf birch is easily distinguishable in UAV imagery from other vegetation due to its growth form.

A ground vegetation survey was carried out in June 2022 to collect land cover data for supervised classification (Land cover survey details in Appendix). Point coordinates of the following land cover classes were collected: barren cover, mixed low-stature vegetation (bog bilberry and crowberry), graminoids, forbs, moss, lichen, and medium-stature shrub (dwarf birch). The point coordinates were collected across sites Gs1 and Gs3. These sites were selected for their representativeness and accessibility. Points were selected based on expertise and judgment of the surveyor, aiming for a representative sample for each class and spatial even distribution. Emphasis was placed on collecting vegetation cover information because vegetation types are more challenging to differentiate than barren cover in the UAV orthomosaics. 160 data points were collected with the Spectra Precision ProMark 120 GPS system. The identified land cover were then used to create training and validation datasets for the classification. As the land cover types were consistent and readily distinguishable across the two ground surveyed sites, we were able to manually select the training data for the other sites from the very-high-resolution orthomosaics of the UAV data. The relatively simple configuration of the landscape - i.e., three distinct and qualitatively different types of land cover - meant that our simplified classification system worked well for our sites.

The following workflow was applied for the classification (Fig. 3):

All processed orthomosaics were clipped to 300 × 300 m, resampled to 5 cm spatial resolution, and merged into one file. We applied the Random Forest (RF) algorithm (Belgiu and Drăguţ, 2016) and trained an individual model using the multi-spectral bands (B, G, R, RE, NIR), the NDVI and the DSM for each of the 12 sites.

The Orfeo ToolBox (OTB) was used in QGIS (3.22) for the classification workflow. Image statistics were computed and included in the model. Training and validation data for each individual class and site was created based on the ground land cover survey and visual interpretation of the very-high-resolution UAV imagery. The RF model was trained with the *TrainImageClassifier,* using default settings.

Afterwards, the *ImageClassifier* was applied using the trained RF model, image statistics and processed layers for each site. Subsequently for accuracy assessment, a Confusion Matrix was computed with the validation data and the F-score and Kappa were calculated for each site (Table 2). Both are established metrics in classification assessment, the F-score, a measure that balances precision and recall, is often used to evaluate the performance of binary classification models. Kappa, or Cohen's Kappa, is a statistic that measures inter-rater reliability for categorical items, comparing the observed agreement with the expected agreement by chance (Campbell, 2011). Finally, a majority filter with a 5 × 5 kernel was applied (using SAGA 7.8.2) to minimise scattered misclassified individual pixels. These datasets were the basis for the following analysis.

Table 2
Results of the percentage of land cover classification for barren, low-stature vegetation (Ls-Veg) and medium-stature shrub (Ms-shrub) classes, and the accuracy of classification.

Percentage land cover and classification precision							
Site	Barren %	F-score	Ls-Veg %	F-score	Ms-shrub %	F-score	Kappa
As	1	0.97	53	0.78	45	0.96	0.82
Gs3	4	0.96	63	0.84	33	0.87	0.83
Sval1	6	0.96	68	0.83	25	0.90	0.85
Gs1	11	0.99	57	0.87	32	0.92	0.87
Reveg	12	0.96	50	0.92	37	0.91	0.89
Gs4	14	0.96	55	0.90	31	0.94	0.89
Gs2	16	0.98	53	0.88	31	0.95	0.90
Sval9	16	0.98	60	0.96	24	0.95	0.95
Sval8	17	0.96	56	0.96	27	0.95	0.94
Sval3	18	0.99	58	0.91	24	0.92	0.90
Sval7	19	0.99	47	0.92	34	0.96	0.92
Sval6	30	0.98	43	0.88	27	0.92	0.90
Mean	14	0.97	55	0.89	31	0.93	0.89

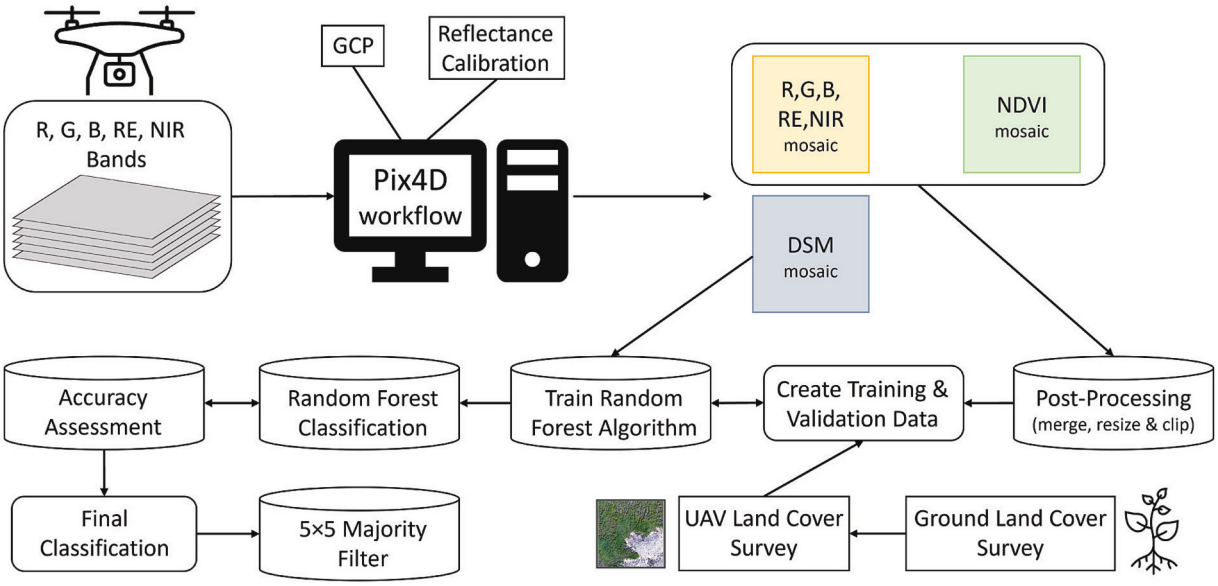

Fig. 3. Workflow for processing and classification of UAV imagery.

The probability density function (PDF) was calculated to estimate the distributions of bare or shrub patch sizes collected from all sites, providing insight into the landscape structure (Moreno-de Las Heras et al., 2011). The PDF gives the probability that a patch has a given area, P (Patch = a). The patch area for each class was calculated using *landscapemetrics* (Hesselbarth et al., 2019) package (1.5.7) in R. Patches were defined that were connected within the eight-neighbor rule. For the PDF, regular bins were created from log-transformed data, with a bandwidth of 0.15. Using log-transformed data has been shown to reduce noise occurring at the tail of the curve and underestimating small values with high frequencies (White et al., 2008).

3.5. NDVI and land cover assessment across sensor scales

To assess the land cover composition for a NDVI value, we compared NDVI pixels for each satellite with the underlying land cover classified from the UAV.

NDVI rasters derived from satellites were clipped to the size of the study sites and vectorized so that each pixel represents a polygon with the NDVI value. Zonal statistics were then calculated for each polygon (representing a NDVI pixel) and the land cover composition within.

3.6. Determination of mixed pixels and the best suitable scale

To compare how different remote sensing datasets capture the landscape we plotted NDVI histograms and visually compared the different remote sensing products for site Sval3. The site was chosen because it has a moderate amount of barren land with patches of different sizes evenly distributed across the landscape.

Each environment has an inherent structure consisting of functional land cover types. These vary in shape, size and position in the landscape. To be able to accurately monitor changes in land cover types, a suitable spatial scale is necessary.

To assess the right spatial scale for our degraded tundra environment, we calculated the Shannon evenness index (SHEI) (Vajda, 1950). SHEI is a diversity metric used in ecology to assess composition and richness in an area (Gergel and Turner, 2017). The function calculates the amount of different land cover types (m) in area and their relative

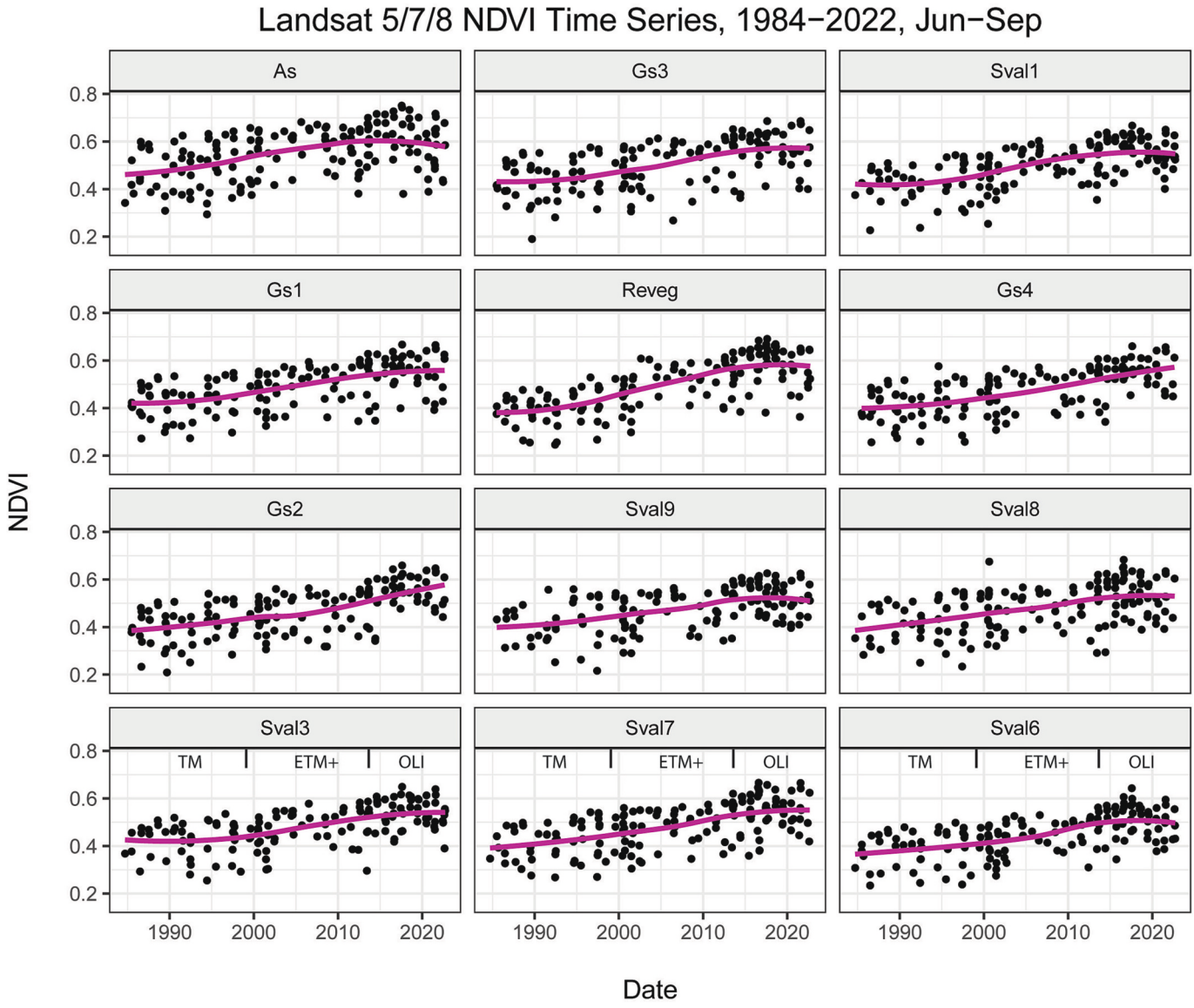

Fig. 4. NDVI time series of all surveyed sites from 1984 until 2022 over the growing season Jun-Sep from Landsat 5/7/8 imagery, ordered from top-left to bottom-right according to increasing barren area. Pixels covered in clouds or shadows were excluded. A steady increasing greening trend is observable. Some sites show a decreasing or lateral trend since 2017. The labels at the bottom of the three lower plots indicate the time periods during which different sensors on Landsat satellites were used: 'TM' for Landsat 5, 'ETM+' for Landsat 7, and 'OLI' for Landsat 8. This delineation is consistent across all plotted sites.

abundances (P_i). It is calculated by dividing the Shannon diversity index (SHDI) by its maximum (h (m)) (Eq. (2)). The output ranges between 0 and 1. In our example, 0 means only one land cover class is present in a pixel and 1 indicates that all land cover classes are present at the same proportional abundance.

SHEI can be calculated as:

$$SHEI = \frac{SHDI}{max(SHDI)} = \frac{\sum_{i=1}^{m}(P_i * ln(P_i))}{ln(m)} \quad (2)$$

The SHEI was calculated for different grid sizes corresponding to different remote sensing spatial resolutions of (0.5, 1, 3, 5, 10, 20, 30, 100, 150) meter. A grid was created with the extent of the studied site and specific spatial resolutions. The SHEI was calculated for each grid cell fully within the area of land cover classification. The mean of all SHEI values for a specific spatial resolution and site was calculated and plotted.

4. Results

4.1. NDVI and land cover trends

Analysis of the NDVI time series reveals a greening trend from 1984 until present for most of the sites (Fig. 4). The sites As, Reveg and Sval6,9 show a slight decline since 2017, while Gs1,3 and Sval1,8 show no change since 2017. The Reveg site was artificially treated with fertiliser and seeds from the early 1990s (Sigurður Þór Guðmundsson, pers. com.) and shows therefore probably a steeper increase in the 1990s and 2000s.

To get a qualitative perspective on long-term land cover changes at our sites, we compared multiple greyscale aerial photographs - downloaded from the Land Surveying Service in Iceland (lmi.is) (Table A5 in Appendix) - with recent UAV imagery. The images cover the study area in July 1980, with an image resolution of ~ 0.73 m per pixel. To illustrate the changes in land cover in the study region, an example area was selected at Sval3, for visual comparison. The historical aerial photo was manually co-registered, using six GCPs and a 2nd order polynomial transformation to the UAV image.

At several locations in Sval3 it can be observed that previously vegetated areas have turned into barren land (Fig. 5, yellow arrow). Further expansion of shrub cover is also visible, though more difficult to distinguish (red arrow). Densification of vegetation cover and secondary regrowth of eroded patches could also contribute to a greening trend, but this is not visible in the comparison.

4.2. Land cover classification and landscape characteristics

Overall, the RF classification showed good accuracies with kappa values > 0.8 (Table 2). An example of a classified site (Sval3) is shown with the corresponding RGB image (Fig. 6). The F-score for the low-stature vegetated class returned the lowest values among the classes with average values around 0.84. The highest F-score at Sval8 and Sval9 was derived from a boggy area where extensive, uniform graminoid cover was classified easily by the model (Table 2). Lower F-values resulted from homogeneous vegetation cover which was harder to classify.

Due to the late stage of the growing season during the UAV survey, the leaves of some shrubs had turned yellow, mainly observed on a few shrubs in site As, which resulted in some misclassification. Shading effects were mainly caused by thúfurs; this also caused some misclassifications where non-shrubby vegetation was assigned to the shrub class. The shrub class showed high accuracies. This is attributed to the contrast between the shrubs and surrounding vegetation, in terms of stature and texture. The relatively high NDVI values of the low-growing deciduous shrub bog bilberry and graminoids, resulted in some minor misclassification as the shrub class. The barren class achieved highest scores (Table 2), attributed to the comparatively strong correlation to NDVI and NIR.

The sizes of barren and shrub patches varied greatly among the sites ranging from 0.0025 m^2 (pixel resolution) to 7045 m^2 for barren patches (with the largest one found in the most eroded site, Sval6), and 0.0025 m^2 to 18,864 m^2 for shrub patches (the largest of which were found in the least eroded site, As). In contrast, at the sites As and Gs3 the largest

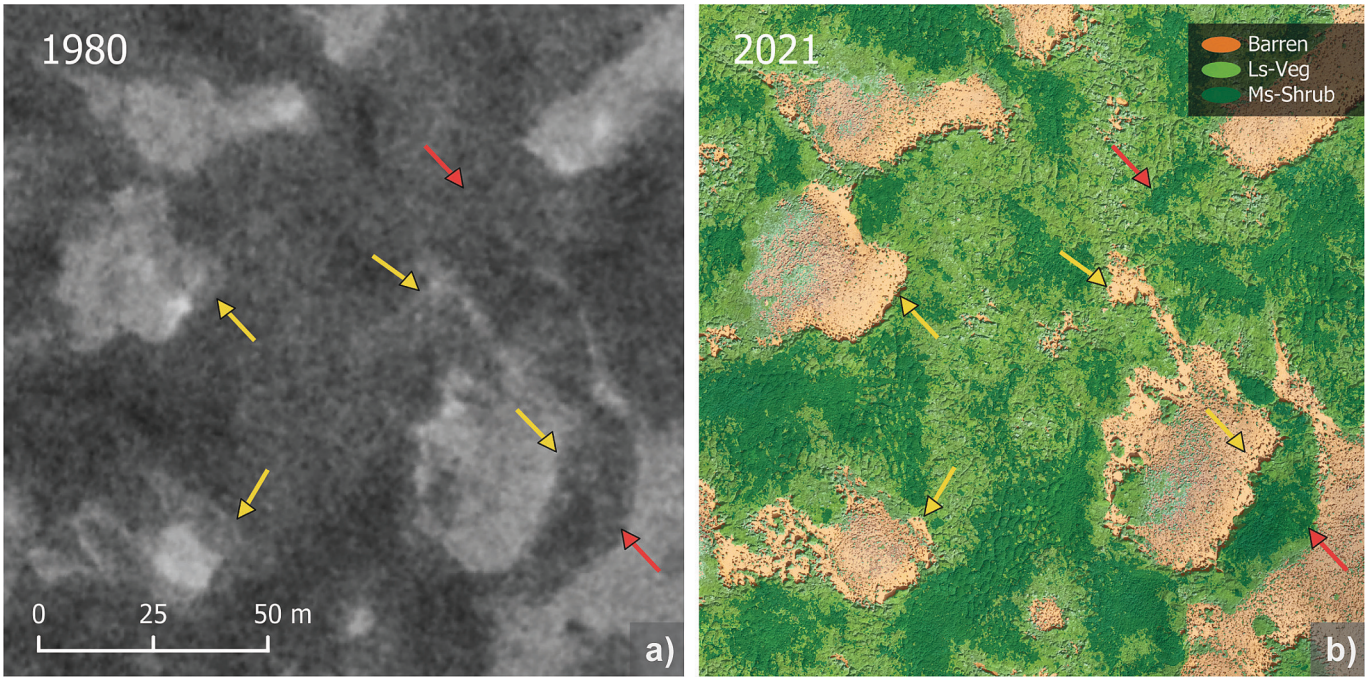

Fig. 5. Comparison of site Sval3 of a) a monochrome aerial photograph (taken in July 1980) with (b) RGB UAV imagery (taken in August 2021) overlaid with a classified land cover map. In panel a) the dark shaded areas represent shrub cover, grey represents vegetation cover and light grey barren areas. Visible changes in texture and tone likely caused by soil erosion is indicated by yellow arrows; red arrows indicate shrub expansion. The arrows are at the same location in both images. (For interpretation of the references to colour in this figure legend, the reader is referred to the web version of this article.)

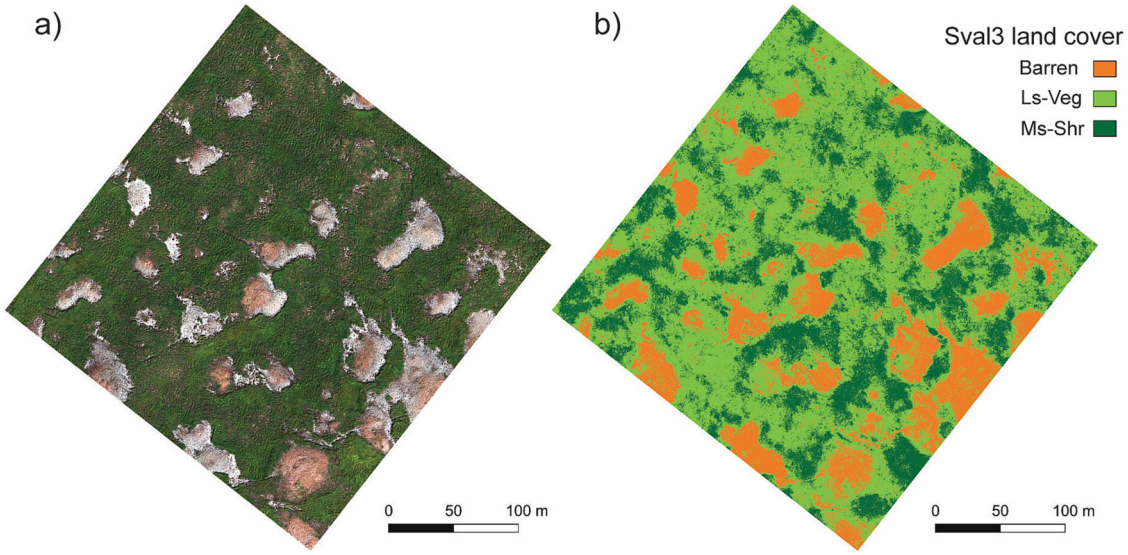

Fig. 6. Site Sval3 a) UAV RGB image b) classified land cover.

barren patches reached only up to 370 m^2 and 379 m^2, respectively, and the largest shrub patch in Sval1 was 824 m^2 (Table 3).

The PDF for low eroded (≤6%) and high eroded (>10%) sites followed different distribution patterns. In contrast, the PDFs for the shrub class had similar distribution patterns across all sites (Fig. 7). The patch size analysis demonstrated that a significant majority of barren and shrub patches fell below the detectability threshold for most satellite platforms (as indicated by the dashed lines in Fig. 7). Specifically, 83% of the shrub patches and 78% of the eroded patches were below the 0.5 m threshold. At 3 m spatial resolution, around 2% of barren and shrub patches were the same size or larger than the pixel size, while with 10 m spatial resolution, only 0.3%. At 30 m resolution, 0.2% in high eroded areas and 0.025% in low eroded areas and 0.06% for shrubs were higher than the pixel size.

The PDF of barren and shrub patches show an upward trend from the smallest patch size (one pixel 0.0025 m^2) to a peak size of about 0.1 m^2 for shrub patches and 0.04 m^2 for barren patches. It should be noted that the majority filter reduced the number of the smallest patch sizes, which explains the initial upward trend. Beyond these sizes, the probability decreases with increasing patch size until 100 m^2, at which point the distribution patterns of low eroded and high eroded areas begin to diverge. Low eroded areas experience a further decline in patch probability, while high eroded areas maintain a consistent probability up to a size of 1000 m^2, followed by a decline. Shrub patches exhibit a smooth decreasing trend, with patch sizes in the upper range exceeding 10,000 m^2 (Fig. 5).

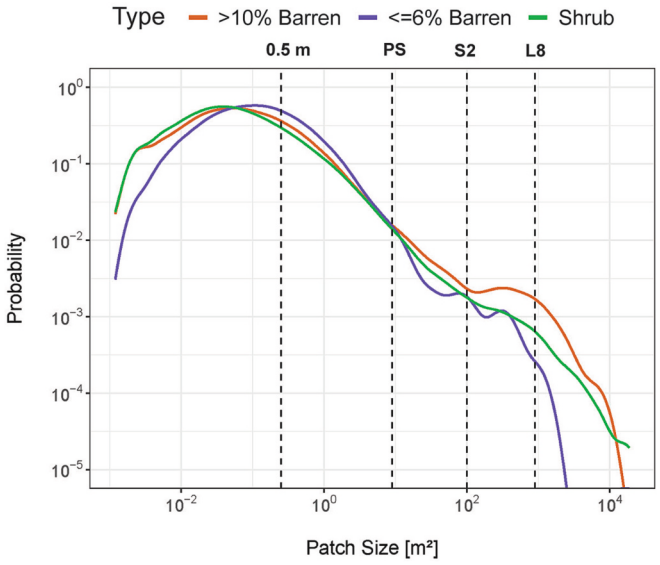

Fig. 7. Probability density function for patch sizes. Dashed lines show the spatial resolution for 0.5 m pixel, PlanetScope (PS), Sentinel-2 (S2) and Landsat (LS).

Table 3
Mean NDVI values for each site and remote sensing dataset. Additionally, the total barren and medium-stature shrub (Ms-Shrub) area, the largest and mean barren and Ms-shrub patch size is shown.

	As	Gs3	Sval1	Gs1	Reveg	Gs4	Gs2	Sval9	Sval8	Sval3	Sval7	Sval6
UAV	0.74	0.7	0.64	0.67	0.68	0.68	0.64	0.63	0.66	0.66	0.66	0.57
PS	0.83	0.78	0.73	0.75	0.72	0.73	0.73	0.68	0.7	0.7	0.69	0.63
S2	0.77	0.73	0.68	0.7	0.69	0.69	0.68	0.66	0.68	0.66	0.69	0.61
L8	0.74	0.78	0.73	0.75	0.73	0.74	0.74	0.70	0.72	0.71	0.74	0.67
Total Barren %	1	4	6	11	12	14	16	16	17	18	19	30
Total Ms-Shrub %	45	33	25	32	37	31	31	24	27	24	34	27
Barren max patch size [m^2]	370	379	1005	2133	3521	1884	2568	1748	6886	2303	2465	7045
Barren mean patch size [m^2]	0.43	0.91	0.68	1.55	1.52	2.48	2.2	1.5	2.72	3.68	2.38	3.14
Ms-Shrub max patch size [m^2]	18,864	1742	824	2014	7619	6057	3538	3730	14,650	1480	6063	2867
Ms-Shrub mean patch size [m^2]	1.79	1.02	0.6	1.17	1.93	1.43	1.68	1.32	1.83	1.09	1.89	1.13

4.3. Variations in NDVI across sensor scales

The mean NDVI values are similar for UAV, PS, S2 and L8 platforms to a certain extent (Table 3). However, PS showed consistently higher values between 0.3 and 0.9 NDVI compared to UAV. S2 mostly matched or slightly exceeded the UAV values of 0.2–0.3 NDVI. L8 data exhibited higher values of 0.5–1.0 NDVI, with the exception of site As, which can be explained by the scene acquisition earlier in the growing season (Table A1 in Appendix).

Mean NDVI values of each site do not always correlate well with proportions of land cover. This can be seen by comparing Sval1 (0.64 NDVI, Barren 6%, Ms-Shrub 25%), Gs2 (0.64 NDVI, Barren 16%, Ms-Shrub 31%) and Sval7 (0.66 NDVI, Barren 19%, Ms-Shrub 34%). For these three sites, mean NDVI value was essentially the same, whilst the relative proportion of barren and shrub cover varied. However, shrub cover didn't always correlate exactly with NDVI as seen on Sval3 (0.66 NDVI, Barren 18%, Ms-Shrub 24%) and Sval7 (0.66 NDVI, Barren 19%, Ms-Shrub 34%). This might be attributed to the proportion of plants with high NDVI values in the Ls-Veg class.

The NDVI map comparison illustrates how different remote sensing (RS) products resolve a fragmented and eroded landscape (Fig. 8a). The patchiness and distribution of the barren areas are clearly visible in the UAV image. With increasing scale, the smaller patches become less apparent, although they are still visible to a certain extent at PS resolution, which shows low contrast between barren and vegetated areas. Larger patches are still visible in the S2 scene, although the edges of the barren patches are blended with the vegetation cover. In the L8 scene, only large barren patches are evident in the lower part. The rest of the barren patches in the centre of the area are not visible.

The UAV NDVI histogram exhibited a wide range of 0.92 and a bimodal distribution, which is not reflected in the satellite data (Fig. 8b). NDVI values from S2 showed the highest dynamic range - 0.58 - compared to PS and L8 that had a similar narrow range of approximately 0.4, despite the large difference in spatial resolution. While PS and L8 showed similar maximum NDVI values to S2, the NDVI lower values were not represented (Fig. 8b).

4.4. Correspondence between land cover and NDVI

All RS products displayed a similar pattern of correspondence of NDVI values to percentage of land cover (PLC), although they differed significantly in their dispersion (Figs. 9; A2, A3 in Appendix).

The NDVI to land cover distribution is explained in more detail for S2, as it correlated best between PLC and NDVI, had the highest dynamic range and a sufficient number of pixels (Fig. 9). NDVI values of fully barren pixels ranged from 0.15 to 0.38, LS-Veg ranged from 0.6 to 0.72, and Ms-Shrub ranged from 0.8 to 0.86 (Fig. 9a, b, c). As the barren cover decreased, the NDVI gradually increased until it reached 0.6, representing the absence of barren cover (Fig. 9a). The plot for the Ls-Veg class showed a peak at the centre of the NDVI spectrum (Fig. 9b). Before and beyond this range, there was a sharp drop in vegetated coverage, suggesting an increase in PLC of Barren cover and Ms-Shrub. No Ms-Shrub cover was observed up to an NDVI of 0.4, after which there was a slight increase in PLC up to 0.68 (Fig. 9c). Thereafter, the PLC increased sharply until it reached its maximum extent.

It is noteworthy, that due to the wide vertical dispersion, a value of 0.6 NDVI could represent 0% or up to 62% barren cover. In Fig. 9d, three sample pixels are shown that have the same NDVI with very different land cover compositions. Vertical dispersion is highest for the Ls-Veg class at 0.66 and Ms-Shrub at 0.76. Large variability at this range for the Ls-Veg is influenced by varying degrees of Barren and Ms-Shrub cover. The large dispersion of Ms-Shrub could be related to plants that were misclassified from the Ls-Veg class with different NDVI values.

Horizontal dispersion varied across the classes and was highest for the Ls-Veg class at 50% PLC ranging from 0.4 to 0.8 NDVI. This was expected as various plants with different spectral reflectance characteristics were included in the class. The dispersion for the Barren class at 50% PLC was 0.4–0.63 NDVI, while for the Ms-Shrub class, was the lowest, ranging between 0.7 and 0.8 NDVI.

L8 plot showed very similar pattern to S2, but they did not include NDVI values < 0.3. This is likely influenced by the insufficient amount of pure Barren cover pixels. The PS also didn't show any NDVI values < 0.35 and had large vertical dispersion at 0.6 NDVI for Barren and Ls-Veg class and at 0.75 for Ls-Veg and Ms-Shrub class (Figs. A2, A3 in Appendix).

4.5. Correspondence between sensor grain-size and land cover

The mean SHEI landscape metric showed a rapid increase up to 3 m and a slow increase at larger spatial resolutions (dashed line in Fig. 10). The mean reached the vertical asymptote at 0.5 m, with the lowest mean SHEI score 0.34. Sites with low and high amounts of barren cover differed in their pattern.

The moderately to highly barren sites from Gs1 onwards followed a similar pattern with SHEI continuously increasing with spatial resolution. At a scale up to 3 m, the SHEI increased sharply to 0.6 and then rose moderately up to 50 m with values > 0.8. Subsequently the SHEI is increased slowly, reaching a horizontal asymptote at 100 m.

The values for sites with low barren cover rose sharply from 0.5 m, eventually peaking at 3 m with 0.65–0.7 SHEI for Gs1, Sval1 and Gs3. Values for site As continued to increase up to 20 m reaching 0.8. Thereafter, the sites levelled off at 50 m at 0.7 SHEI (Table A6 in Appendix).

5. Discussion

We set out to 1) explore the biases occurring from satellite monitoring in degraded Arctic landscapes and 2) determine which spatial resolution is most useful in evaluating vegetation cover and landscape health in fragmented tundra landscapes. We found that shrubification can lead to spectral confusion, which can obscure soil erosion processes, and confirmed the importance of considering multiple spatial scales when monitoring land condition in Iceland. GróLind, Iceland's first long-term vegetation and soil monitoring program, was initiated in 2017 and uses satellite imagery, UAVs, and on-site analyses to estimate land condition and predict areas at risk (Marteinsdóttir et al., 2017; Arnalds, 2015). Our findings should give confidence that the use of 10 m resolution S2 data will result in a sufficient accurate indication of land condition (although ≤ 3 m resolution would be better), but suggests that the use of coarser resolution products may be problematic due to the difficulties of mixed spectral signatures and the potential for masking increases in barren cover.

5.1. NDVI time series

The mean NDVI has increased on our study sites over the last four decades (Fig. 4). This greening trend could indicate an amelioration of the environment, an increase in vegetation cover and a decrease in barren land. There has been an overall greening of tundra vegetation across the circumpolar Arctic in the last four decades and a direct link between warming air temperatures and vegetation greening has been reported (Meredith et al., 2019; Raynolds et al., 2013; Myers-Smith et al., 2011; Bhatt et al., 2010). However, the comparison of aerial images from 1980 and a recent UAV image (Fig. 5) shows that soil erosion continued on our study sites, which was evident on all study plots when comparing aerial photographs, i.e. vegetation cover was lost across the region in that time period.

If the increase in NDVI we observed was not due to increased vegetated area, it must have been caused by changes in vegetation structure and composition. Studies have demonstrated correlations among greenness in the Arctic with air temperature and aboveground biomass (Bhatt et al., 2017; Ju and Masek, 2016; Xu et al., 2013), and prolonged

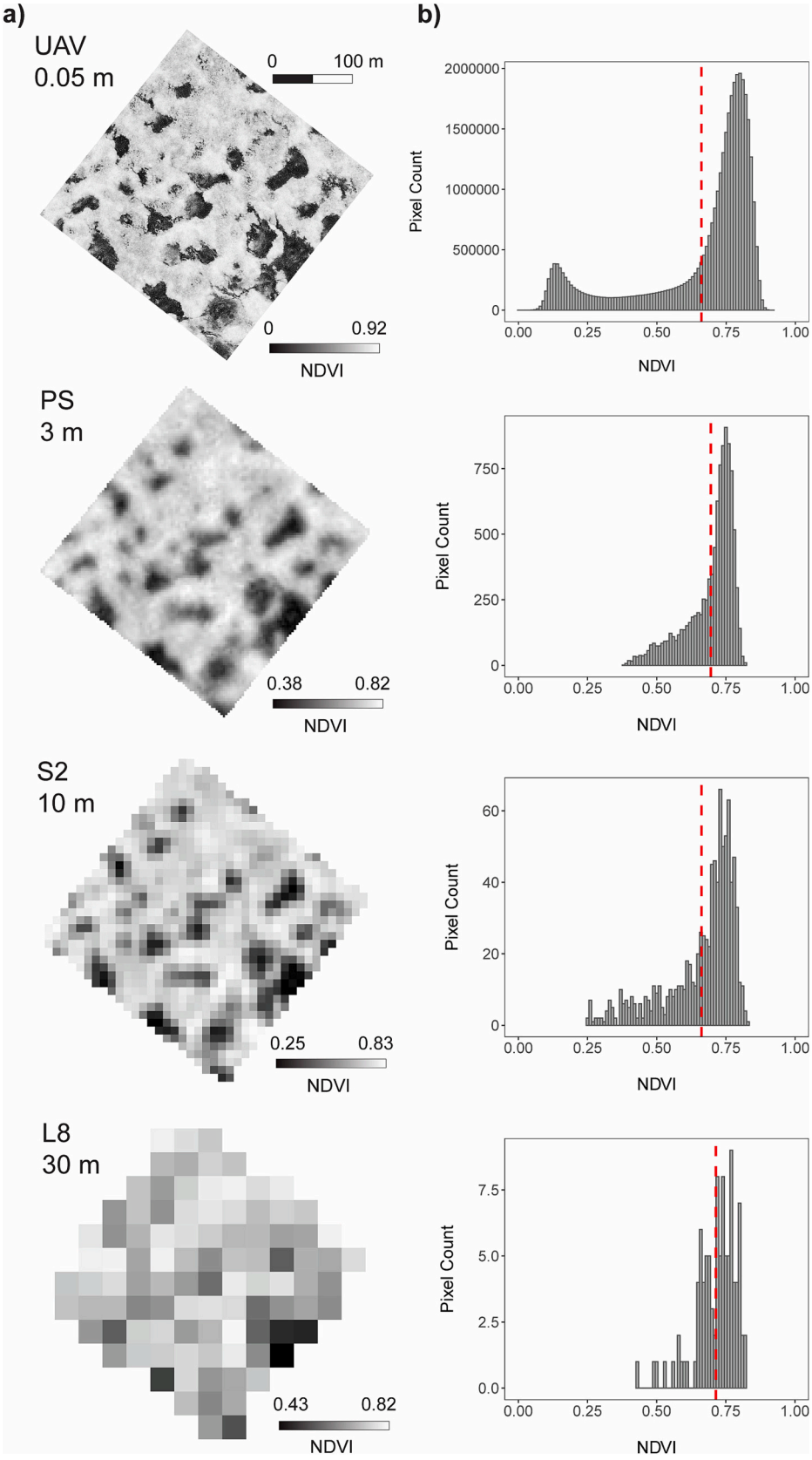

Fig. 8. a) NDVI landscape and b) histogram comparison between different remote sensing datasets from site Sval3. The red dashed vertical line indicates the mean NDVI. (For interpretation of the references to colour in this figure legend, the reader is referred to the web version of this article.)

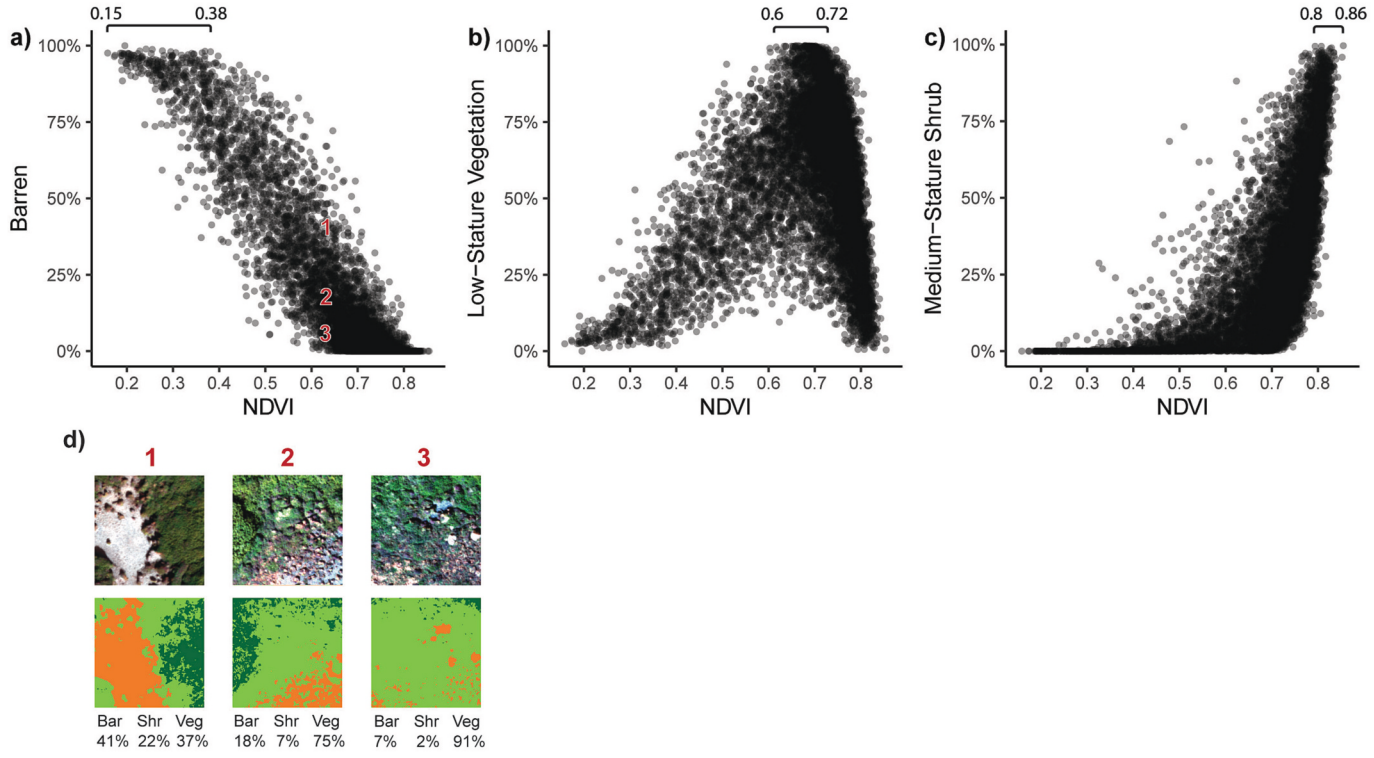

Fig. 9. Representation of Sentinel-2 (S2) NDVI pixels and corresponding percentage of land cover (PLC) classified from UAV. Each datapoint represents a S2 pixel plotted from all sites. The lines above show the NDVI range for fully covered pixels per land cover. a) For Barren, b) Ls-Veg and c) Ms-Shrub cover. d) Upper panel RGB image, lower panel land cover classification, for three selected pixels of edge length 10 m with NDVI value of 0.61. The sample pixels illustrate a large variability in land cover composition for a specific NDVI value. The pixels are highlighted in the Barren graph Fig. 9a.

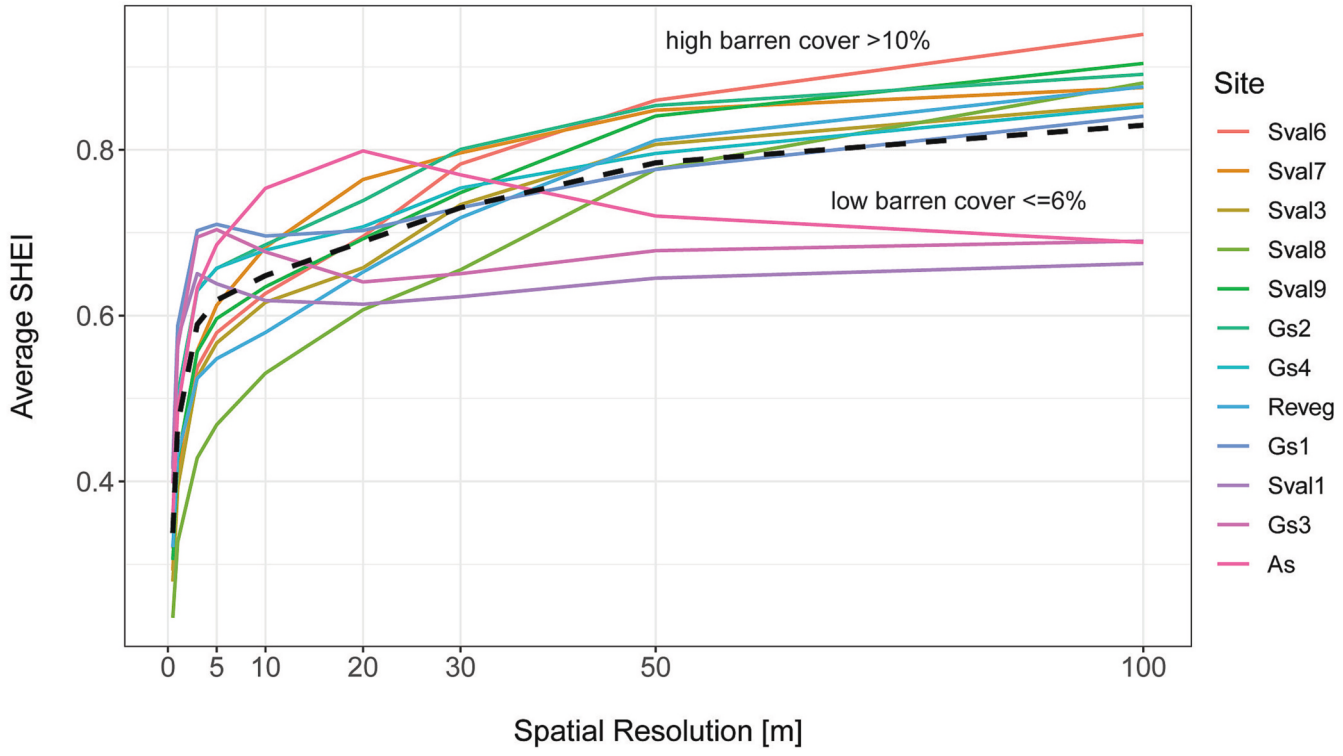

Fig. 10. Graph showing SHEI for different sites and spatial scales. The sites in the legend are sorted by decreasing barren cover. The black dashed line is the mean of all sites.

growing seasons that are shifting plant phenology (Post et al., 2018; Oberbauer et al., 2013).

On our sites, the NDVI values of the shrub class were found to be higher than those of the surrounding vegetation (Fig. 9). Combined with our observations indicating shrub growth (Fig. 5), with other studies demonstrating that shrub growth in the Arctic tundra was closely linked to spectral greening (Pattison et al., 2015; Fraser et al., 2014; Forbes et al., 2010), leads us to conclude that the increasing NDVI trend at our sites was mainly driven by the expansion of shrub patches.

This time series has a low spatial resolution (size of study sites, 300 × 300 m), encompassing various erosion patches and vegetation cover across the entire study site. It underscores the significance of pixel resolution relative to the patch size, revealing that when pixel resolution exceeds the studied patch dimensions, the spectral confusion of distinct land covers, as erosion and shrub patches, hinders the detection of land cover changes. This confusion arises as multiple concurrent trends either counteract one another, or a dominant trend (shrubification) obscures a weaker signal (soil erosion).

5.2. Land cover and NDVI correspondence

Overall, L8, S2, and PS returned similar figures for Barren, Ls-Veg and Ms-Shrub cover, but differed significantly in their dispersion of PLC vs NDVI, as dynamic range (Figs. 8, 9, Table 3) and minor changes in the mean NDVI.

Surprisingly, the percentage of land cover classified as barren exhibited a higher degree of dispersion (Fig. 9a) than expected, considering the distinct spectral differences in NDVI between vegetated and non-vegetated surfaces. This could be related to the broader definition of barren land, which could have included biocrust and different stages of soil deflation in barren land types, leading to some variability in that class (Fig. 2e, f).

The satellite platforms returned a very wide range of values for the Ls-Veg class (Fig. 9b). This is because this class encompasses many different plant types - including low-growing, deciduous and evergreen shrubs, graminoids, forbs and mosses - each with their own distinct spectral characteristics. Sub-dividing this class might help to reduce variance in future analyses. However, this would be challenging in Iceland because the vegetation cover displays high alpha (plot-level) diversity but low beta (between-plot) diversity. In other words, a diversity of plant species at a fine spatial scale combines to form homogeneous vegetation at a landscape scale.

The dynamic range provides an indication of how much information is retained and differs significantly among the RS products. PS and L8 had a low dynamic range, mainly missing the lower NDVI values (Fig. 8b) compared to S2, leading to lower contrasting imagery which limits its use for accurate classification of land cover and deriving biophysical parameters. No satellite image was able to detect the bimodal distribution visible in the UAV histogram (Fig. 8b).

We observed high dispersion of NDVI vs PLC, which was strongest for PS. For regional scale (10s km^2) studies this dispersion can average out, however for landscape scale (100 s m^2) studies with coarser resolutions this dispersion could skew interpretation of the data. This is notable for L8 data (Fig. A2a in Appendix), that displayed a 60% difference in Barren cover among pixels with a narrow range of NDVI values (0.54–0.55).

The mean NDVI values varied slightly across the RS datasets, with S2 resembling the UAV values most closely (Table 3). Various factors, such as band-pass differences among sensors (Ke et al., 2015), bidirectional reflectance influenced by viewing angles (Song and Woodcock, 2003), and differences in acquisition dates, could contribute to the observed variations in NDVI values. Slight differences in acquisition dates can have a significant impact in Arctic locations due to the short growing season (Myers-Smith et al., 2020). This explains the consistently higher NDVI values in the L8 data, which are 2–3 weeks earlier and closer to the peak growing season compared to the UAV acquisition, except for site As (2 days difference to UAV acquisition) which had the same value as the UAV. The variability in PS data can be either related to the sensor quality, affected by the varying viewing angles of PS platforms, which varied between 1 and 5°, or differences in NIR and R spectral ranges (Table 1). Frazier and Hemingway (2021) demonstrated that the radiometric and geometric quality of PS imagery doesn't match that of traditional systems such as Landsat and Sentinel-2, and it is not always "analysis ready," often requiring additional correction and post-processing. Hence, Sentinel-2 data can be the better choice even though the spatial resolution is lower.

5.3. Mixed pixel and spatial resolution

The second aim of the study was to identify the most appropriate spatial resolution to study a degraded Icelandic tundra environment. In doing so, we assessed the effectiveness of commonly used remote sensing datasets in detecting geomorphologically relevant land cover categories.

We chose to categorise three functional land cover types and these categories proved effective in our study environment. It's important to note that one of our categories - eroded terrain - has limited extent across the Arctic. While our land cover classification may need adaptation to areas that lack eroded terrain, the analytical approach using SHEI to assess spatial resolution remains the same. The importance of spatial resolution can be illustrated by comparing the mean SHEI metrics calculated for lower eroded areas (barren cover $\leq$ 6%) and higher eroded areas (barren cover $>$ 10% of total). Both types of terrain exhibit sharp rises in SHEI as spatial resolution increased, up to a size of $\sim$ 3 m (Fig. 10). At larger spatial resolutions, mean SHEI diverged. On lower eroded areas, mean SHEI peaked at spatial resolutions of 3–5 m, declined slightly, then levelled-out; on lower eroded terrain, mean SHEI kept increasing to an asymptote at 100 m spatial resolution.

SHEI is a metric of the diversity of cover within a grid cell. Low SHEI values indicate low diversity, i.e., overwhelming dominance of a single cover type. High SHEI values indicate a variety of cover types with approximately equal proportional coverage. Thus, we expect low SHEI values with small grid cells (the cells can only encompass a single cover type) and increases in SHEI as spatial resolution decreases and increasingly large grid cells encompass multiple, contrasting patches.

On our sites, SHEI increased predictably with spatial resolution for the higher eroded areas. Finer spatial resolutions only detected one land cover type and mean SHEI is low; mean SHEI increased as larger grid cells encompassed both barren and vegetated cover, until the resolution approximated the size of the largest patches and increasing the grid dimension did not capture any further diversity.

On the less eroded sites, variation within the vegetation cover - particularly the presence of small patches of shrubs - led to a different pattern. Small spatial resolution still resulted in low mean SHEI. But a spatial resolution around 3 m was able to encompass small patches of shrubs and barren terrain, leading to a peak in mean SHEI at these scales. As spatial resolution decreased, the cells became dominated by non-shrubby vegetation and mean SHEI decreased.

Our study demonstrates the limitations of coarse resolution datasets for studying complex ecological-geomorphology processes such as soil erosion at a landscape scale. The Landsat data (30 m resolution) proved inadequate for detecting small-scale vegetation changes (shrub expansion) and the emergence of small erosion patches, as these features were merged in a single mixed pixel (Fig. 8a). Furthermore, our research indicates that SHEI based on high-resolution imagery could be a valuable tool for understanding land cover change.

5.4. Remote sensing recommendations for soil erosion monitoring

Monitoring the extent of barren cover from coarse resolution satellite products is challenging, especially in a fragmented Arctic landscape. Our study demonstrated the importance of considering spatial resolution

when assessing soil erosion and vegetation change. Landsat spatial resolution is not sufficient to capture important ecological and geomorphological changes. Using inappropriate datasets with coarse spatial resolution may result in underestimation of the extent of soil erosion and crucial threshold-crossing events being missed.

High-resolution information on sub-pixel heterogeneity is essential for accurate interpretations. Integration of UAV imagery with field knowledge provides a valuable solution by capturing data at a scale comparable to ground based observations. This approach enhances the comprehension of spectral variations at coarse spatial resolutions, by validating satellite datasets and facilitating the development of scaling functions. Ultimately, this enables more precise and reliable long-term monitoring of land cover change. This is in line with Sotille et al. (2020), where the authors compared S2, L8 and UAV-derived data in a study of Antarctic vegetation cover. In their study, the use of UAV data improved the accuracy of vegetation cover estimation, due to higher spatial resolution and greater discrimination of areas that appeared to be homogeneous in lower resolution imagery.

Newer satellite platforms will assist with efforts to monitor soil erosion and vegetation change in a warming Arctic, due to higher spatial resolutions, availability of multiple spectral bands and spatial coverage. Studies have shown that S2 and PS are more effective in detecting the extent of vegetation cover compared to L8 (Andreatta et al., 2022). The use red-edge bands – available in S2 and PS – permits the accurate separation of barren and vegetation cover, allowing for more accurate mapping capabilities (Andreatta et al., 2022; Fernández et al., 2022). Caution should be taken in the selection of PS products due to variations in radiometric and geometric quality (Frazier and Hemingway, 2021) and lower dynamic range.

However, even platforms such as S2 or PS might not be sufficient to monitor the development of small shrub/erosion patches, which are critical for environmental assessment in Iceland (Cutler et al., 2023; Streeter and Cutler, 2020). The dynamic behavior of small patches can be an indicator of important ecological/geomorphological processes, revealing potential tipping points in the landscape development that may not be apparent in widely used RS products due to their limited spatial resolution. Very-high-resolution imagery, like that from the Pléiades Neo mission and WorldView 3/4, offers the potential to pan-sharpen multispectral imagery from 1.2 to 0.3 m spatial resolution and to study small-scale land cover changes more accurately on a local scale.

Clearly, each RS platform has its advantages and disadvantages. The future of remote sensing will lie in the combination of various systems. PS is useful in resolving small-scale features on a local scale, but shortcomings in consistent image quality limit its use for spectrally complex land cover discrimination and time series analysis. Landsat will continue to be an important dataset for long-term time series analysis along with Visible Infrared Imager-Radiometer Suite (VIIRS), Sentinel-3 OLCI and Moderate Resolution Imaging Spectroradiometer (MODIS) for monitoring large areas. Caution should be taken when interpreting large-scale monitoring studies in locations where small-scale ecological and geomorphological processes scale-up to landscape-level features. In the long-term, the S2 mission is likely to prove the best platform for tundra environmental monitoring, as it offers frequent image acquisition, excellent sensors, and variety of spectral bands at suitable spatial resolutions. To enhance reliability of coarse satellite datasets in highly fragmented environments, we recommend complementing it with UAV imagery for validation.

6. Conclusion

Soil erosion poses a significant threat to affected regions in the Arctic tundra and should be closely monitored to prevent landscapes crossing irreversible tipping points. However, risks are involved when using unsuitable satellite platforms. In this study, we were able to show that inappropriate spatial resolutions can indicate an improvement in landscape condition despite ongoing vegetation cover loss. In Landsat data, most of the erosion patches are masked within a mixed pixel, which doesn't allow accurate monitoring. PlanetScope has more suitable spatial resolution, but low spectral dynamic range and variability in data acquisition quality limit its use, despite being a valuable additional dataset. Sentinel-2 performed best, showing good agreement of NDVI values to the UAV data, good spectral dynamic range and a sufficient spatial resolution to resolve larger barren patches.

To the best of our knowledge, we used for the first time the Shannon evenness index to evaluate pixel mixture. This method could provide useful information in assessing what spatial resolutions are appropriate when monitoring different environments. Further testing of this metric with different landscape configurations could increase its applicability. In our environment, the amount of information captured increased significantly below 3 m spatial resolution. We therefore emphasize the importance of using UAVs in highly fragmented environments such as the Arctic tundra. The fine-scale variability makes it a difficult terrain to monitor and necessary to validate satellite datasets.

Funding

This research was supported by the St Andrews World Leading Scholarship.

Author contributions

Conceptualization: GK, RS, TB designed the research project. Methodology: GK, RS formulated the methodology. Investigation: GK, RS conducted the UAV surveys. Formal analysis: GK conducted the image processing and data analysis. Visualisation: GK created the graphics. Writing (original draft): GK produced the original draft of the manuscript. Writing (review & editing): all authors contributed to the final version of the manuscript.

Declaration of Competing Interest

The authors have no conflicts of interest to declare. All co-authors have seen and agree with the contents of the manuscript. We certify that the submission is original work and is not under review at any other publication.

Data availability

The data and R code that support the findings of this study are openly available on GitHub at https://github.com/georg-kodl/erosion-scale. UAV-derived orthomosaics and land cover maps underpinning this publication can be accessed at https://doi.org/10.17630/f1e25320-7c79-4876-9719-4c1131cd8ed4 (Kodl and Streeter, 2023). Other remote sensing datasets are publicly available including: Landsat-8 (https://earthexplorer.usgs.gov/), Sentinel-2 (https://dataspace.copernicus.eu/). A specific quota of PlanetScope datasets are freely available for researcher purposed at (https://planet.com). Landsat datasets for NDVI time series are freely accessible through (https://earthengine.google.com/).

Acknowledgements

We would like to thank Hildur Stefánsdóttir and Sigurður Þór Guðmundsson for their hospitality at Grásteinn and the opportunity to conduct field research on their land. We thank Farzaneh Barzegar (Graz University of Technology) for the reviewing of the Landsat-8 data.

Appendix

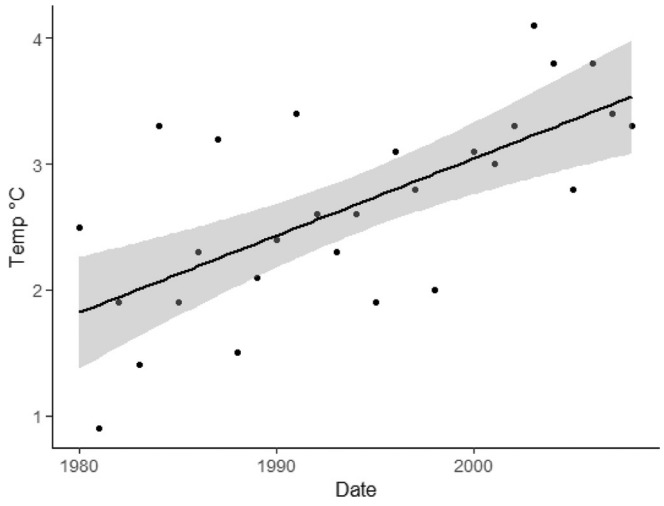

Fig. A1. Temperature change in N-Iceland Raufarhöfn (elevation at sea level) for the period 1980–2008. LOESS curve fitted to mean annual temperature with 95% confidence interval.

Table A1
Name, centroid location of the surveyed sites and date of acquisition for utilised remote sensing imagery. The elevation ranges from the lowest 30 m to the highest 160 m.

Platform			UAV	PlanetScope	Sentinel-2	Landsat-8
Site	Lat	Lon	Date			
Gs1	66.140	−15.495	23/08/21	01/09/21	01/09/21	08/08/21
Gs2	66.141	−15.502	23/08/21	01/09/21	01/09/21	08/08/21
Gs3	66.137	−15.498	23/08/21	01/09/21	01/09/21	08/08/21
Gs4	66.138	−15.504	25/08/21	01/09/21	01/09/21	08/08/21
Reveg	66.175	−15.512	30/08/21	01/09/21	01/09/21	08/08/21
Sval1	66.215	−15.631	30/08/21	01/09/21	01/09/21	08/08/21
Sval3	66.173	−15.727	31/08/21	01/09/21	01/09/21	08/08/21
Sval6	66.154	−15.758	31/08/21	01/09/21	01/09/21	08/08/21
Sval7	66.144	−15.780	01/09/21	01/09/21	01/09/21	08/08/21
Sval8	66.137	−15.781	01/09/21	01/09/21	01/09/21	08/08/21
Sval9	66.113	−15.768	25/08/21	01/09/21	01/09/21	08/08/21
As	66.030	−16.393	02/09/21	01/09/21	01/09/21	31/08/21

Table A2
Satellite datasets downloaded from respective platforms.

Satellite	Product ID	Type	Source
PlanetScope	*20210901_123636_17_2407_3B_AnalyticMS*	*Level 3B*	*planet.com*
	20210901_123638_47_2407_3B_AnalyticMS	*Level 3B*	
	20210901_114920_66_2440_3B_AnalyticMS	*Level 3B*	
Sentinel-2	*S2A_MSIL2A_20210901T130301_N0301_R038_T28WDU_20210901T154212*	*Level 2a*	*dataspace.copernicus.eu*
Landsat-8	*LC08_L2SP_217014_20210808_20210819_02_T1*	*Collection 2, Level 2, Tier 1*	earthexplorer.usgs.gov
	LC08_L2SP_218014_20210831_20210909_02_T1	*Collection 2, Level 2, Tier 1*	

Table A3
Accessed GEE databases for time series analysis.

GEE database
USGS Landsat 8 Collection 2 Tier 1 TOA Reflectance
USGS Landsat 7 Collection 2 Tier 1 TOA Reflectance
USGS Landsat 5 TM Collection 2 Tier 1 TOA Reflectance

UAV survey details

The P4m camera we used, had six imaging 1/2.9" CMOS sensors, five recording monochrome bands (blue (B) at 450 ± 16 nm; green (G) at 560 ± 16 nm; red edge (RE) at 730 ± 16 nm and near-infra red (NIR) at 840 ± 26 nm) and one RGB sensor, all with a global shutter and 2.08 MP (1600 × 1300) resolution. The camera has a field of view of 62.7°, a focal length of 5.74 mm; autofocus was set to ∞ and the aperture to f/2.2. The P4m camera generated results comparable to the widely applied Parrot Sequoia + camera. GCPs were used to georeference the orthomosaic of each site. The mean geolocation error for each GCP in horizontal and vertical directions was about HMRS/VMRS = ~0.5 m. The Mapir reflectance target was imaged before, during and after each survey. The image that best represented the average light conditions during the survey, was used for radiometric correction when generating orthomosaics in Pix4D.

Land cover survey

Georg Kodl carried out a land cover survey in June 2022 to collect point coordinates of land cover types. The survey was conducted at the sites Gs1 and Gs3, for their representativeness and accessibility using a Spectra Precision ProMark 120 GPS system. A judgmental sampling method was applied, wherein land cover were selected based on expertise and judgment, aiming for a representative sampling and spatially equal distribution. Following land cover classes were collected: barren cover, mixed low-stature vegetation (bog bilberry and crowberry), graminoids, forbs, moss, lichen, and medium-stature shrub (dwarf birch). 73 Ls-Veg, 51 Ms-Shrub and 36 Barren data points were collected (160 in total).

Table A4
Flight protocol.

Flight-ID	Altitude [m]	Start	End	GCP	Cloud conditions
Gs1,2	70	12:19	13:51	6	Scattered stratus & cumulus cover - sun partly obscured
Gs3	70	13:53	14:36	8	Stratus - sun obscured
Gs4	70	08:23	09:06	8	Clear sky to haze
Sval9	70	14:20	15:05	6	Haze
Sval1	70	11:03	11:52	6	Cumulus - sun obscured
Reveg	70	14:11	15:26	7	Cumulus - over most sky (alternating with sun)
Sval3	70	10:55	11:55	6	Thin cirrus - sun not obscured
Sval6	70	14:37	15:12	8	Thin cirrus - sun obscured (alternating with sun)
Sval8	70	11:35	12:18	7	Haze
Sval7	70	14:30	15:15	6	Haze
As	70	11:26	12:25	7	Thin cirrus - sun obscured, later half stratus cover

Table A5
Aerial photos used from LMI.

Flight location and path	Photo number	Date
91 - Balafell-Melrakkanes	F-8070	01/07/1980

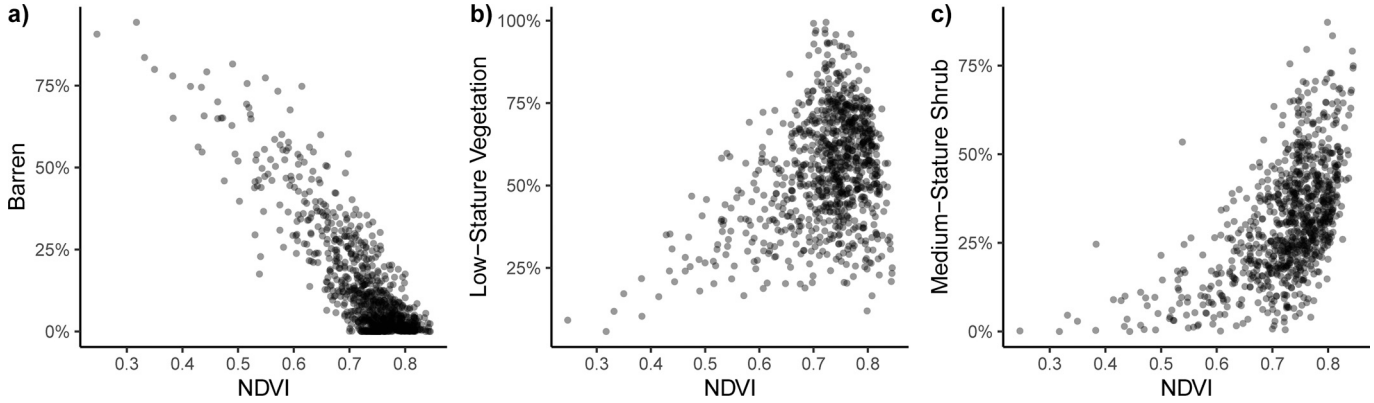

Fig. A2. Representation of L8 NDVI pixel and corresponding PLC classified from UAV. Each datapoint represents a L8 pixel plotted from all sites. a) For Barren, b) Ls-Veg and c) Ms-shrub cover.

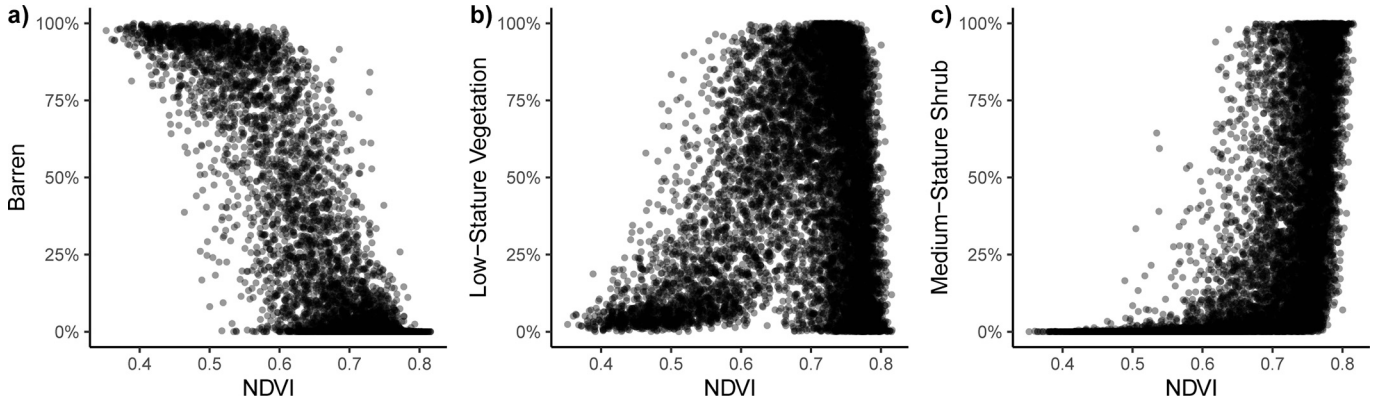

Fig. A3. Representation of PS NDVI pixel and corresponding PLC classified from UAV. Each datapoint represents a PS pixel plotted from site Sval7 a) For Barren, b) Ls-Veg and c) Ms-shrub cover.

Table A6
Mean SHEI values for surveyed sites and different spatial resolutions (from Fig. 10).

Site	Spatial resolution [m]									
	0.5	1	3	5	10	20	30	50	100	150
As	0.36	0.49	0.63	0.69	0.75	0.80	0.77	0.72	0.69	0.66
Gs3	0.40	0.56	0.69	0.70	0.68	0.64	0.65	0.68	0.69	0.70
Sval1	0.41	0.57	0.65	0.64	0.62	0.61	0.62	0.65	0.66	0.65
Gs1	0.42	0.59	0.70	0.71	0.70	0.70	0.73	0.78	0.84	0.83
Reveg	0.32	0.43	0.52	0.55	0.58	0.65	0.72	0.81	0.88	0.82
Gs4	0.35	0.50	0.63	0.66	0.68	0.71	0.75	0.80	0.85	0.83
Gs2	0.36	0.50	0.63	0.66	0.69	0.74	0.80	0.85	0.89	0.83
Sval9	0.31	0.43	0.56	0.60	0.63	0.69	0.75	0.84	0.90	0.94
Sval8	0.24	0.33	0.43	0.47	0.53	0.61	0.66	0.78	0.88	0.99
Sval3	0.28	0.39	0.53	0.57	0.62	0.66	0.73	0.81	0.86	0.91
Sval7	0.29	0.41	0.56	0.61	0.68	0.76	0.80	0.85	0.88	0.87
Sval6	0.32	0.42	0.54	0.58	0.63	0.70	0.78	0.86	0.94	0.99
Mean	0.34	0.47	0.59	0.62	0.65	0.69	0.73	0.78	0.82	0.82

Appendix A. Supplementary data

Supplementary data to this article can be found online at https://doi.org/10.1016/j.rse.2023.113935.

References

Andreatta, Davide, Gianelle, Damiano, Scotton, Michele, Dalponte, Michele, 2022. Estimating grassland vegetation cover with remote sensing: a comparison between Landsat-8, Sentinel-2 and PlanetScope imagery. Ecol. Indic. 141, 109102 https://doi.org/10.1016/j.ecolind.2022.109102.

Arnalds, Olafur, 2015. The Soils of Iceland. Springer Netherlands, Dordrecht.

Assmann, Jakob J., Kerby, Jeffrey T., Cunliffe, Andrew M., Myers-Smith, Isla H., 2019. Vegetation monitoring using multispectral sensors — best practices and lessons learned from high latitudes. J. Unmanned Veh. Syst. 7 (1), 54–75. https://doi.org/10.1139/juvs-2018-0018.

Assmann, Jakob J., Myers-Smith, Isla H., Kerby, Jeffrey T., Cunliffe, Andrew M., Daskalova, Gergana N., 2020. Drone data reveal heterogeneity in tundra greenness and phenology not captured by satellites. Environ. Res. Lett. 15 (12), 125002 https://doi.org/10.1088/1748-9326/abbf7d.

Barrio, Isabel C., Hik, David S., Thórsson, Jóhann, Svavarsdóttir, Kristín, Marteinsdóttir, Bryndís, Jónsdóttir, Ingibjörg Svala, 2018. The sheep in wolf's clothing? Recognizing threats for land degradation in Iceland using state-and-transition models. Land Degrad. Dev. 29 (6), 1714–1725. https://doi.org/10.1002/ldr.2978.

Beamish, Alison, Raynolds, Martha K., Epstein, Howard, Frost, Gerald V., Macander, Matthew J., Bergstedt, Helena, et al., 2020. Recent trends and remaining challenges for optical remote sensing of Arctic tundra vegetation: a review and outlook. Remote Sens. Environ. 246, 111872 https://doi.org/10.1016/j.rse.2020.111872.

Belgiu, Mariana, Drăguţ, Lucian, 2016. Random forest in remote sensing: a review of applications and future directions. ISPRS J. Photogramm. Remote Sens. 114, 24–31. https://doi.org/10.1016/j.isprsjprs.2016.01.011.

Bhatt, Uma S., Walker, Donald A., Raynolds, Martha K., Comiso, Josefino C., Epstein, Howard E., Jia, Gensuo, et al., 2010. Circumpolar Arctic tundra vegetation change is linked to sea ice decline. Earth Interact. 14 (8), 1–20. https://doi.org/10.1175/2010EI315.1.

Bhatt, Uma S., Walker, Donald A., Raynolds, Martha K., Bieniek, Peter A., Epstein, Howard E., Comiso, Josefino C., et al., 2017. Changing seasonality of panarctic tundra vegetation in relationship to climatic variables. Environ. Res. Lett. 12 (5), 55003. https://doi.org/10.1088/1748-9326/aa6b0b.

Campbell, James B., 2011. Introduction to Remote Sensing, 5th ed. Guilford Press, New York, London.

Cutler, Nick A., Kodl, Georg, Streeter, Richard T., Thompson, Polly I.J., Dugmore, Andrew J., 2023. Soil moisture, stressed vegetation and the spatial structure of soil erosion in a high latitude rangeland. Eur. J. Soil Sci. 74 (4), e13393 https://doi.org/10.1111/ejss.13393.

Dugmore, Andrew J., Gisladóttir, Gudrún, Simpson, Ian A., Newton, Anthony, 2009. Conceptual models of 1200 years of Icelandic soil erosion reconstructed using tephrochronology. J. N. Atl. 2, 1–18. https://doi.org/10.3721/037.002.0103.

Eichel, Jana, Corenblit, Dov, Dikau, Richard, 2016. Conditions for feedbacks between geomorphic and vegetation dynamics on lateral moraine slopes: a biogeomorphic feedback window. Earth Surf. Process. Landf. 41 (3), 406–419. https://doi.org/10.1002/esp.3859.

Fernández, D., Adermann, E., Pizzolato, M., Pechenkin, R., Rodríguez, C.G., 2022. Remote mapping of soil erosion risk in Iceland. Int. Arch. Photogramm. Remote. Sens. Spat. Inf. Sci. 135–141. https://doi.org/10.5194/isprs-archives-XLVIII-4-W1-2022-135-2022. XLVIII-4/W1-2022.

Forbes, Bruce C., Fauria, Marc Macias, Zetterberg, Pentti, 2010. Russian Arctic warming and 'greening' are closely tracked by tundra shrub willows. Glob. Chang. Biol. 16 (5), 1542–1554. https://doi.org/10.1111/j.1365-2486.2009.02047.x.

Fraser, Robert H., Lantz, Trevor C., Olthof, Ian, Kokelj, Steven V., Sims, Richard A., 2014. Warming-induced shrub expansion and lichen decline in the Western Canadian Arctic. Ecosystems 17 (7), 1151–1168. https://doi.org/10.1007/s10021-014-9783-3.

Frazier, Amy E., Hemingway, Benjamin L., 2021. A technical review of planet smallsat data: practical considerations for processing and using PlanetScope imagery. Remote Sens. 13 (19), 3930. https://doi.org/10.3390/rs13193930.
Fretwell, Peter T., Convey, Peter, Fleming, Andrew H., Peat, Helen J., Hughes, Kevin A., 2011. Detecting and mapping vegetation distribution on the Antarctic Peninsula from remote sensing data. Polar Biol. 34 (2), 273–281. https://doi.org/10.1007/s00300-010-0880-2.
Gergel, Sarah E., Turner, Monica G., 2017. Learning Landscape Ecology. https://doi.org/10.1007/978-1-4939-6374-4.
Giri, Chandra, Pengra, Bruce, Long, J., Loveland, Thomas R., 2013. Next generation of global land cover characterization, mapping, and monitoring. Int. J. Appl. Earth Obs. Geoinf. 25, 30–37. https://doi.org/10.1016/j.jag.2013.03.005.
Heindel, Ruth C., Culler, Lauren E., Virginia, Ross A., 2017. Rates and processes of aeolian soil erosion in West Greenland. Holocene 27 (9), 1281–1290. https://doi.org/10.1177/0959683616687381.
Hesselbarth, Maximilian H.K., Sciaini, Marco, With, Kimberly A., Wiegand, Kerstin, Nowosad, Jakub, 2019. Landscapemetrics: an open-source R tool to calculate landscape metrics. Ecography 42 (10), 1648–1657. https://doi.org/10.1111/ecog.04617.
Ju, Junchang, Masek, Jeffrey G., 2016. The vegetation greenness trend in Canada and US Alaska from 1984–2012 Landsat data. Remote Sens. Environ. 176, 1–16. https://doi.org/10.1016/j.rse.2016.01.001.
Ke, Yinghai, Im, Jungho, Lee, Junghee, Gong, Huili, Ryu, Youngryel, 2015. Characteristics of Landsat 8 OLI-derived NDVI by comparison with multiple satellite sensors and in-situ observations. Remote Sens. Environ. 164, 298–313. https://doi.org/10.1016/j.rse.2015.04.004.
Kemppinen, Julia, Niittynen, Pekka, Virkkala, Anna-Maria, Happonen, Konsta, Riihimäki, Henri, Aalto, Juha, Luoto, Miska, 2021. Dwarf shrubs impact tundra soils: drier, colder, and less organic carbon. Ecosystems 24 (6), 1378–1392. https://doi.org/10.1007/s10021-020-00589-2.
Kemppinen, Julia, Niittynen, Pekka, Happonen, Konsta, Roux, Peter C., Aalto, Juha, Hjort, Jan, et al., 2022. Geomorphological processes shape plant community traits in the Arctic. Glob. Ecol. Biogeogr. https://doi.org/10.1111/geb.13512. Article geb.13512.
Kodl, Georg, Streeter, Richard T., 2023. Multispectral UAV imagery and land cover maps of tundra rangeland in north-eastern Iceland, Aug-Sep 2021 (dataset). University of St Andrews Research Portal, St Andrews. https://doi.org/10.17630/f1e25320-7c79-4876-9719-4c1131cd8ed4.
Laidler, Gita J., Treitz, Paul M., Atkinson, David M., 2008. Remote sensing of Arctic vegetation: relations between the NDVI, spatial resolution and vegetation cover on Boothia peninsula, Nunavut. ARCTIC 61 (1), 1. https://doi.org/10.14430/arctic2.
Landsat collection 2, 2021. Version 1.0: January 7, 2021; Version 1.1: January 15, 2021. With assistance of U.S. Geological Survey. Reston, VA (Fact Sheet, 2021–3002). Available online at. https://pubs.usgs.gov/publication/fs20213002.
Lara, Mark J., Nitze, Ingmar, Grosse, Guido, Martin, Philip, McGuire, A. David, 2018. Reduced arctic tundra productivity linked with landform and climate change interactions. Sci. Rep. 8 (1), 2345. https://doi.org/10.1038/s41598-018-20692-8.
Marston, Richard A., 2010. Geomorphology and vegetation on hillslopes: interactions, dependencies, and feedback loops. Geomorphology 116 (3–4), 206–217. https://doi.org/10.1016/j.geomorph.2009.09.028.
Marteinsdóttir, Bryndís, Barrio, Isabel C., Jónsdóttir, Ingibjörg Svala, 2017. Assessing the ecological impacts of extensive sheep grazing in Iceland. IAS 30, 55–72. https://doi.org/10.16886/IAS.2017.07.
Martin, Andrew C., Jeffers, Elizabeth S., Petrokofsky, Gillian, Myers-Smith, Isla, Macias-Fauria, Marc, 2017. Shrub growth and expansion in the Arctic tundra: an assessment of controlling factors using an evidence-based approach. Environ. Res. Lett. 12 (8), 85007. https://doi.org/10.1088/1748-9326/aa7989.
McFadden, Joseph P., Chapin, F. Stuart, Hollinger, David Y., 1998. Subgrid-scale variability in the surface energy balance of arctic tundra. J. Geophys. Res. Atmos. 103 (D22), 28,947–28,961. https://doi.org/10.1029/98JD02400.
Meredith, M., Sommerkorn, M., Cassotta, S., Derksen, C., Ekaykin, A., Hollowed, A., Kofinas, G., Mackintosh, A., Melbourne-Thomas, J., Muelbert, M.M.C., Ottersen, G., Pritchard, H., Schuur, E.A.G., 2019. Polar regions. In: IPCC Special Report on the Ocean and Cryosphere in a Changing Climate.
Moreno-de Las Heras, Mariano, Saco, Patricia M., Willgoose, Garry R., Tongway, David J., 2011. Assessing landscape structure and pattern fragmentation in semiarid ecosystems using patch-size distributions. Ecol. Appl.: Publ. Ecol. Soc. Am. 21 (7), 2793–2805. https://doi.org/10.1890/10-2113.1.
Myers-Smith, Isla H., Hik, David S., 2018. Climate warming as a driver of tundra shrubline advance. J. Ecol. 106 (2), 547–560. https://doi.org/10.1111/1365-2745.12817.
Myers-Smith, Isla H., Forbes, Bruce C., Wilmking, Martin, Hallinger, Martin, Lantz, Trevor, Blok, Daan, et al., 2011. Shrub Expansion in Tundra Ecosystems: Dynamics, Impacts and Research Priorities.
Myers-Smith, Isla H., Kerby, Jeffrey T., Phoenix, Gareth K., Bjerke, Jarle W., Epstein, Howard E., Assmann, Jakob J., et al., 2020. Complexity revealed in the greening of the Arctic. Nat. Clim. Chang. 10 (2), 106–117. https://doi.org/10.1038/s41558-019-0688-1.
Niittynen, Pekka, Heikkinen, Risto K., Aalto, Juha, Guisan, Antoine, Kemppinen, Julia, Luoto, Miska, 2020. Fine-scale tundra vegetation patterns are strongly related to winter thermal conditions. Nat. Clim. Chang. 10 (12), 1143–1148. https://doi.org/10.1038/s41558-020-00916-4.
Oberbauer, S.F., Elmendorf, S.C., Troxler, T.G., Hollister, R.D., Rocha, A.V., Bret-Harte, M.S., et al., 2013. Phenological response of tundra plants to background climate variation tested using the international tundra experiment. Philos. Trans. R. Soc. Lond. Ser. B Biol. Sci. 368 (1624), 20120481. https://doi.org/10.1098/rstb.2012.0481.
Pattison, Robert R., Jorgenson, Janet C., Raynolds, Martha K., Welker, Jeffery M., 2015. Trends in NDVI and tundra community composition in the Arctic of NE Alaska between 1984 and 2009. Ecosystems 18 (4), 707–719. https://doi.org/10.1007/s10021-015-9858-9.
Post, Eric, Steinman, Byron A., Mann, Michael E., 2018. Acceleration of phenological advance and warming with latitude over the past century. Sci. Rep. 8 (1), 3927. https://doi.org/10.1038/s41598-018-22258-0.
Post, Eric, Alley, Richard B., Christensen, Torben R., Macias-Fauria, Marc, Forbes, Bruce C., Gooseff, Michael N., et al., 2019. The polar regions in a 2°C warmer world. Sci. Adv. 5 (12), eaaw9883 https://doi.org/10.1126/sciadv.aaw9883.
Rantanen, Mika, Karpechko, Alexey Yu, Lipponen, Antti, Nordling, Kalle, Hyvärinen, Otto, Ruosteenoja, Kimmo, et al., 2022. The Arctic has warmed nearly four times faster than the globe since 1979. Commun. Earth Environ. 3 (1) https://doi.org/10.1038/s43247-022-00498-3.
Raynolds, Martha K., Walker, Donald A., Verbyla, David, Munger, Corinne A., 2013. Patterns of change within a tundra landscape: 22-year Landsat NDVI trends in an area of the northern foothills of the Brooks Range, Alaska. Arct. Antarct. Alp. Res. 45 (2), 249–260. https://doi.org/10.1657/1938-4246-45.2.249.
Rietkerk, Max, Dekker, Stefan C., de Ruiter, Peter C., van de Koppel, Johan, 2004. Self-organized patchiness and catastrophic shifts in ecosystems. Science (New York, N.Y.) 305 (5692), 1926–1929. https://doi.org/10.1126/science.1101867.
Siewert, Matthias B., Olofsson, Johan, 2020. Scale-dependency of Arctic ecosystem properties revealed by UAV. Environ. Res. Lett. 15 (9), 94030. https://doi.org/10.1088/1748-9326/aba20b.
Song, C., Woodcock, C.E., 2003. Monitoring forest succession with multitemporal Landsat images: factors of uncertainty. IEEE Trans. Geosci. Remote Sens. 41 (11), 2557–2567. https://doi.org/10.1109/TGRS.2003.818367.
Sotille, Maria E., Bremer, Ulisses F., Vieira, Gonçalo, Velho, Luiz F., Petsch, Carina, Simões, Jefferson C., 2020. Evaluation of UAV and satellite-derived NDVI to map maritime Antarctic vegetation. Appl. Geogr. 125, 102322 https://doi.org/10.1016/j.apgeog.2020.102322.
Stow, Douglas A., Hope, Allen, McGuire, David, Verbyla, David, Gamon, John, Huemmrich, Fred, et al., 2004. Remote sensing of vegetation and land-cover change in Arctic tundra ecosystems. Remote Sens. Environ. 89 (3), 281–308. https://doi.org/10.1016/j.rse.2003.10.018.
Streeter, Richard T., Cutler, Nick A., 2020. Assessing spatial patterns of soil erosion in a high-latitude rangeland. Land Degrad. Dev. 31 (15), 2003–2018. https://doi.org/10.1002/ldr.3585.
Tape, Ken D., Hallinger, Martin, Welker, Jeffrey M., Ruess, Roger W., 2012. Landscape heterogeneity of shrub expansion in Arctic Alaska. Ecosystems 15 (5), 711–724. https://doi.org/10.1007/s10021-012-9540-4.
Thorsson, Johann, 2008. Desertification of High Latitude Ecosystems: Conceptual Models, Time-Series Analyses and Experiments (PhD thesis). Texas A&M University.
Vajda, S., 1950. The mathematical theory of communication. By Claude E. Shannon and Warren Weaver. Pp. 117 $2.50. 1949. (University of Illinois Press, Urbana). Math. Gaz. 34 (310), 312–313. https://doi.org/10.2307/3611062.
Veðurstofa Íslands, 2022. Climatological Data. Icelandic Meteorological Office. Retrieved from. http://en.vedur.is/climatology/data/http://en.vedur.is/climatology/data/.
Virtanen, Tarmo, Ek, Malin, 2014. The fragmented nature of tundra landscape. Int. J. Appl. Earth Obs. Geoinf. 27, 4–12. https://doi.org/10.1016/j.jag.2013.05.010.
Walker, Donald A., Raynolds, Martha K., Daniëls, Fred J.A., Einarsson, Eythor, Elvebakk, Arve, Gould, William A., et al., 2005. The circumpolar Arctic vegetation map. J. Veg. Sci. 16 (3), 267–282. https://doi.org/10.1111/j.1654-1103.2005.tb02365.x.
Weijers, Stef, Myers-Smith, Isla H., Löffler, Jörg, 2018. A warmer and greener cold world: summer warming increases shrub growth in the alpine and high Arctic tundra. Erdkunde 72 (1), 63–85. Available online at. https://www.jstor.org/stable/26411580.
White, Ethan P., Enquist, Brian J., Green, Jessica L., 2008. On estimating the exponent of power-law frequency distributions. Ecology 89 (4), 905–912. Available online at. http://www.jstor.org/stable/27651627.
Xu, L., Myneni, R.B., Chapin, Iii, F.S., Callaghan, Terry, V., Pinzon, J.E., Tucker, Compton, J., Zhu, Z., et al., 2013. Temperature and vegetation seasonality diminishment over northern lands. Nat. Clim. Chang. 3 (6), 581–586. https://doi.org/10.1038/nclimate1836.
Yang, Dedi, Meng, Ran, Morrison, Bailey D., McMahon, Andrew, Hantson, Wouter, Hayes, Daniel J., et al., 2020. A multi-sensor unoccupied aerial system improves characterization of vegetation composition and canopy properties in the Arctic tundra. Remote Sens. 12 (16), 2638. https://doi.org/10.3390/rs12162638.